Numerical and Experimental Study of Overtopping and Failure of Rockfill Dams

Antonia Larese[1]; Riccardo Rossi[2]; Eugenio Oñate[3]; Miguel Ángel Toledo[4]; Rafael Morán[5]; and Hibber Campos[6]

Abstract: This paper aims to present and validate a numerical technique for the simulation of the overtopping and onset of failure in rockfill dams caused by mass sliding. This goal is achieved by coupling a fluid dynamic model for the simulation of the free surface and through-flow problems together with a numerical technique for the calculation of the rockfill response and deformation. Both the flow within the dam body and in its surroundings are taken into account. An extensive validation of the resulting computational method is performed by solving several failure problems on physical models of rockfill dams for which experimental results have been obtained by the authors. **DOI: 10.1061/(ASCE)GM.1943-5622.0000345.** © *2014 American Society of Civil Engineers.*

Author keywords: Overtopping; Rockfill dams; Seepage; Slope failure.

Introduction

Climate change and amplification of extreme weather events in recent years has led to the need for an increased safety level of critical structures to protect against natural hazards. In this context, a category that is likely to be affected by extreme flooding events is represented by dams and dikes. For this reason, many countries have already activated a revision of the design criteria, and furthermore, there is a rising interest in new techniques that can help a predictive study of the structural response during extreme events.

According to the International Commission on Large Dams (ICOLD) (1995), exceptional flooding represents the more crucial cause of failure of embankment dams. In fact, although an overspill does not easily affect the integrity of concrete dams, in the case of rockfill dams, it often leads to the complete failure of the downstream slope.

Unfortunately, the history of dam failures caused by overtopping is long and dramatic. The failure of the Banquiao Dam caused by

[1]Researcher, Centre Internacional de Mètodes Numèrics en Enginyeria, 08034 Barcelona, Spain; Associate Lecturer, Technical Univ. of Catalonia (UPC BarcelonaTech), 08034 Barcelona, Spain (corresponding author). E-mail: antoldt@cimne.upc.edu

[2]Researcher, Centre Internacional de Mètodes Numèrics en Enginyeria, 08034 Barcelona, Spain; Associate Lecturer, Technical Univ. of Catalonia (UPC BarcelonaTech), 08034 Barcelona, Spain.

[3]Director, Centre Internacional de Mètodes Numèrics en Enginyeria, 08034 Barcelona, Spain; Associate Lecturer, Technical Univ. of Catalonia (UPC BarcelonaTech), 08034 Barcelona, Spain.

[4]Professor, Dept. of Civil Engineering, Hydraulics and Energy, Escuela Técnica Superior de Ingenieros de Caminos, Canales y Puertos, Technical Univ. of Madrid, 28040 Madrid, Spain.

[5]Researcher, Dept. of Civil Engineering, Hydraulics and Energy, Escuela Técnica Superior de Ingenieros de Caminos, Canales y Puertos, Technical Univ. of Madrid, 28040 Madrid, Spain.

[6]Researcher, Dept. of Civil Engineering, Hydraulics and Energy, Escuela Técnica Superior de Ingenieros de Caminos, Canales y Puertos, Technical Univ. of Madrid, 28040 Madrid, Spain.

Typhoon Nina in 1975 is a catastrophe that illustrates the magnitude of these occurrences. This failure triggered the collapse of another 62 dams in the same basin. This resulted in approximately 62,000 deaths caused by the flood and 145,000 deaths caused by famine and epidemics. Another example is the failure of the Tous Dam in Valencia in October 1982, causing a tsunami of 20 million cubic meters of water that flowed in the Comunidad Valenciana. These and many other similar historical events demonstrate that, when the water exceeds the crest of the dam, the consequences can be catastrophic. An exceptional flooding seriously compromises the structure and brings, in almost all cases, its failure. Nevertheless, the breaching formation is a relatively slow process and never leads to a sudden explosive failure. Chanson (2009) reported that, in the case of the Glashütte Dam, the complete failure of the structure occurred 4 h after the beginning of the overtopping. In the case of the Teton Dam, the reservoir was drained after approximately 12 h. When the water overpasses the crest of the dam, overtopping starts, and a seepage process begins in the downstream slope, leading to its progressive saturation. Resistance is not instantaneously compromised, but it is progressively reduced. There are two main failure mechanisms: mass sliding and superficial erosion (Toledo 1997, 1998). The first is a loss of stability in a part of the downstream region caused by the landslide. This is the predominant failure mechanism when the downstream slope is very steep. The saturation of the rockfill leads to a reduction of effective stresses that, together with seepage, induce the formation of a failure circle along the whole width of the dam that abruptly crumbles. Conversely, superficial erosion is predominant when the downstream slope is flat ($1V$:$3H$ for instance). Water coming out from the toe of the dam drags away the superficial rocks, leading to the formation of channels in the downstream slope.

The clay core represents an additional barrier before the complete failure of the structure once the protection given by the rockfill is no longer present. Its failure can be the consequence of different mechanisms that are outside the scope of this paper.

The aim of this work is to focus on the seepage effects on the rockfill and to analyze the formation and evolution of the breach. To do this, a numerical tool capable of simulating the evolution of the flux throughout the rockfill and its consequences on the rockfill response is presented and validated.

The computational model combines traditional finite elements with more recent particulate analysis techniques for the seepage-free

surface simulation and the dam structural response, respectively. In fact, the authors developed an Eulerian computational fluid dynamic (CFD) code using a level set technique for tracking the evolution of the free surface and the seepage flow with a unified formulation. A viscoplastic model is proposed for computing the structural response via a Lagrangian framework using the particle FEM (PFEM) (Idelsohn et al. 2004; Larese et al. 2008; Oñate et al. 2011b), which is a particle technique that allows following the large deformation of the rockfill during failure in a natural way.

An extensive validation of the accuracy and usefulness of the computational model and the numerical tool is presented using data from experiments on physical models of rockfill dams.

All the algorithms presented in this paper have been implemented in the open-source object-oriented multiphysical analysis platform *KRATOS* available at http://kratos.cimne.upc.edu (Dadvand et al. 2010).

Numerical Approach

Both problems (the seepage and the onset and evolution of failure in the dam body) are solved using a continuum mechanics approach. A Eulerian fluid model is combined with a Lagrangian structural one to minimize the computational effort for the fluid calculation in the Eulerian framework and to naturally follow the large deformation of the rockfill material.

Lagrangian algorithms are traditionally used in structural mechanics where each node of the computational mesh follows the associated material particle evolution. This makes it easy to track the interface between fluid and structure and to consider materials with history-dependent constitutive relations. Their weakness is the inability to follow large distortions of the domain without the need of a continuum remeshing, which leads to a difficult parallelization of the code. Eulerian algorithms, on the other hand, are largely used in fluid dynamics because of the ease of following large movements. In this case, the computational mesh is fixed, and the continuum moves with respect to the grid; therefore, an interface tracking technique is required to follow the evolution of the free surface (Donea and Huerta 2003).

Taking into account these considerations, the model presented in this paper is composed of three modules:

- A free-surface Eulerian fluid model able to consider the presence of a porous medium and to handle variable discharge conditions. This kinematic framework is chosen to minimize the computational cost of the CFD simulation. Moreover, the edge-based parallel algorithm, presented by Rossi et al. (2013), is implemented and adapted to the problem of interest to speed up the solution.

- A Lagrangian structural model to simulate the behavior of a rockfill slope in presence (or not) of variable hydrodynamic forces. The chosen technique is PFEM because it has been successfully used in several applications that include large domain deformation and detaching particles. This is useful to model the separation of solid particles from the bed surface and to follow their subsequent motion as individual particles with a known density, an initial acceleration, and velocity subject to gravity forces (Oñate et al. 2004, 2006).

- A coupling tool to integrate the Eulerian and Lagrangian models to simulate the transient process during failure of a rockfill slope caused by exceptional flooding. For this purpose, a tool to map variables between nonmatching meshes was developed (Larese 2012).
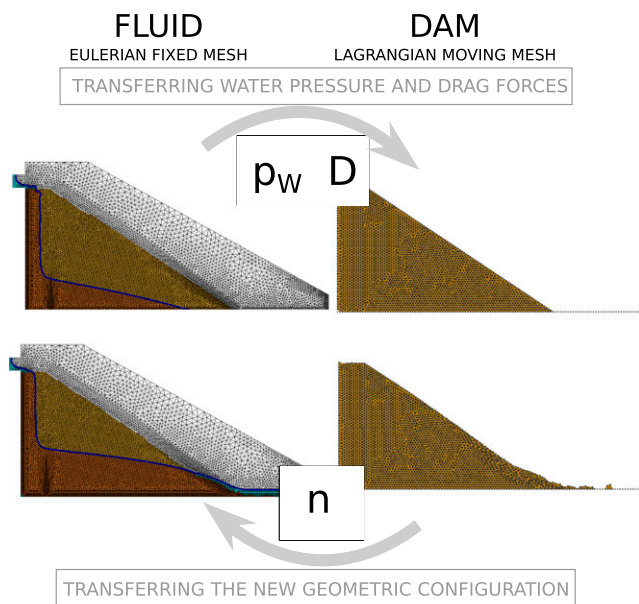

Fig. 1. Graphical summary of the FSI solution process (Springer and Computational Mechanics, vol. 50, 2012, pp. 805–819, "A coupled PFEM-Eulerian approach for the solution of porous FSI problems," Larese, A., Rossi, R., Oñate, E., and Idelsohn, S. © *Computational Mechanics*, with kind permission from Springer Science and Business Media)
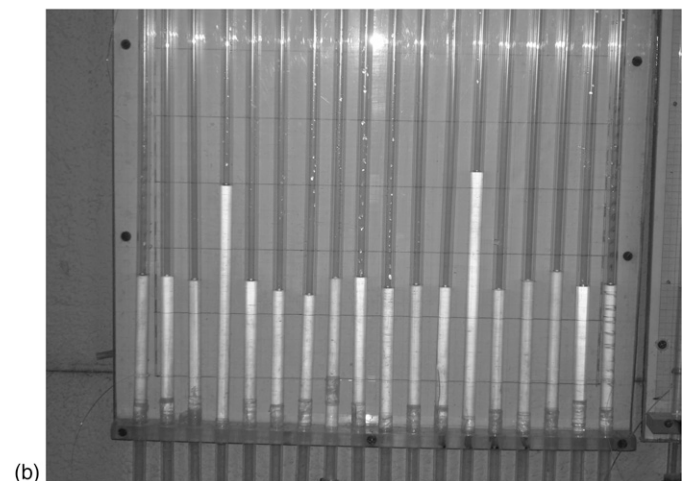

Fig. 2. Pressure instrumentation: (a) front view of UPM channel with the pressure sensors tubes; (b) one of the panels for reading pressure heights (images by authors)

In the following sections, the balance equations for the fluid and the structural problems are presented, and the numerical approach is briefly explained. The implementation details can be found in Larese (2012), Larese et al. (2012), and Rossi et al. (2013).

Fluid Problem

The CFD module has been conceived as a tool to treat free surface flows with a transient incoming condition, and it has been modified to be able to take into account the presence of a porous medium within the same formulation. The only boundary condition imposed strongly is the inlet of water; no boundary conditions are needed at the outflow (i.e., a zero boundary pressure is implicitly imposed) or at the entrance of the porous material. The spatial distribution of porosity n ($n = 1$ outside the rockfill and $n \neq 1$ inside) is the only needed information to be set in preprocess.

Traditionally, depth-integrated models are extensively used for analyzing the flux in porous media application (Hansen and Roshanfekr 2012); nevertheless, these approaches are often limited to the stationary case, or they need the downstream point at which water emerges to be known a priori (Hansen 1992). An interesting approach to treat the seepage flow caused by unsteady boundary conditions can be found in Fu and Jin (2009). In this case, the authors focus only on the porous media flow and consider the saturation level and the water head as variables of the problem. This leads to the need of coupling the equations of the unsaturated domain with those of the saturated one. Conversely, several authors simulate the free surface flows using the Stokes equation and the seepage flow using Darcy's law (Urquiza et al. 2008; Discacciati et al. 2002; Chen et al. 2011). All these approaches require careful treatment of the interface conditions between the porous media and the free surface flows.
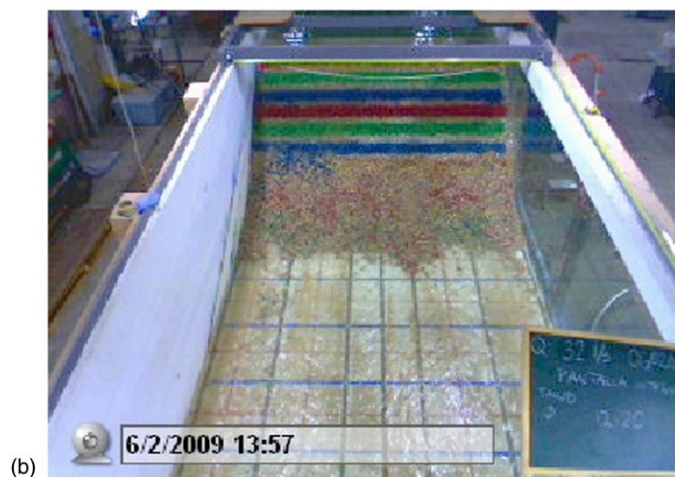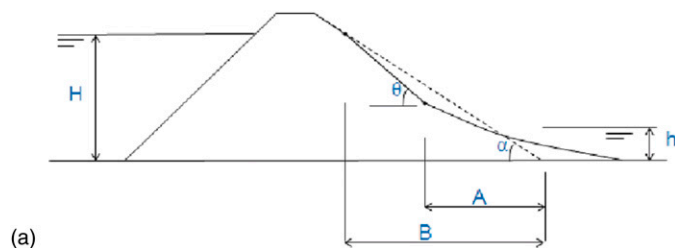
In the present work, water is treated as a Newtonian incompressible viscous fluid, and the equations governing water flow in a porous medium are a modified form of the traditional Navier-Stokes equations. The details of the derivation of both the balance of linear momentum and the balance of mass equations can be found in Larese (2012). A similar formulation was used by Nithiarasu et al. (1997) for the treatment of the convective flux in a cavity with variable porosity, and it was chosen for the present work because it allows the simulation of the free surface and seepage flows with a unique formulation once the porosity distribution in space has been defined.
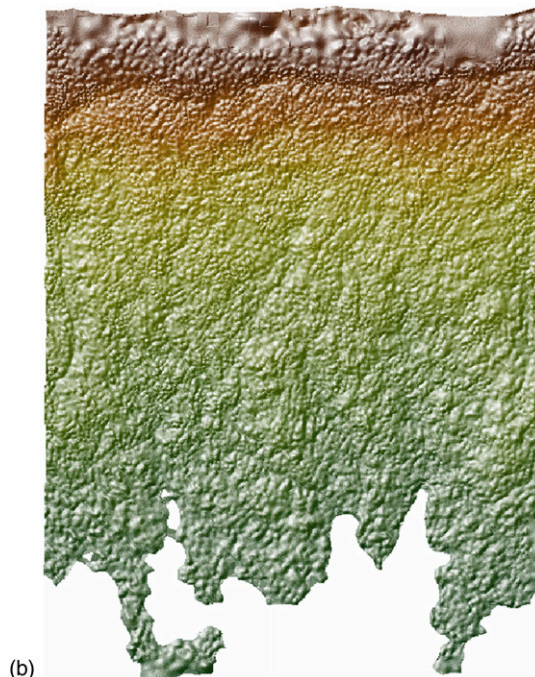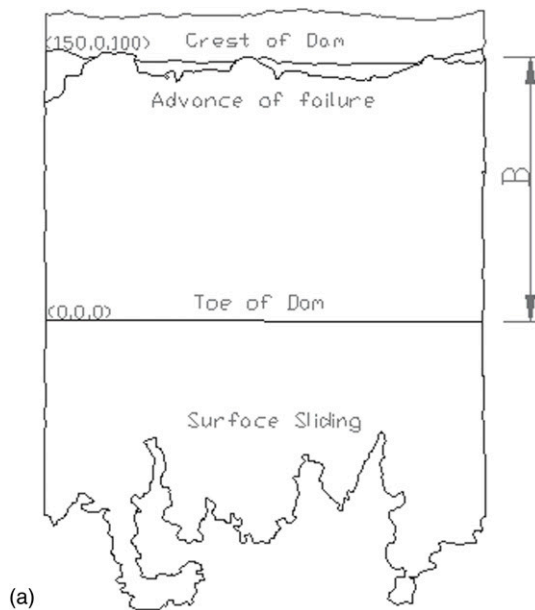

(a)

Fig. 3. Advance of failure; characterization and measurement setup: (a) schematic view; (b) measurement of the advance of failure (image by authors)

(a)

(b)

Fig. 4. Advance of failure; digital model of the deformed slope to evaluate the evolution of the advance of failure B: (a) advance of failure in the digital model; (b) digital layout

The governing equations of the fluid are

$$\rho_f \partial_t \mathbf{u} + \rho_f \overline{\mathbf{u}} \cdot \nabla \mathbf{u} + n\nabla p - 2\nabla \cdot \mu \nabla^s \mathbf{u} - \rho_f n\mathbf{b} + n\mathbf{D} = 0$$

$$\text{in} \quad \Omega, t \in (0, T) \tag{1}$$

$$\nabla \cdot \mathbf{u} = 0 \quad \text{in} \quad \Omega, t \in (0, T)$$

In the previous equations, the degrees of freedom (DOFs) of the problem are the Darcy velocity $\mathbf{u}$ and the fluid pressure p. The Darcy velocity is the fluid velocity averaged over the total control volume Ω (often called macroscopic velocity or unit discharge being the discharge per unit volume), whereas the fluid velocity $\overline{u}$ is averaged over the empty part of Ω (called Ω_E). Their relation is stated by the Dupuit-Forchheimer equation (Nield and Bejan 1992)

$$\mathbf{u} = n\overline{\mathbf{u}} \tag{2}$$

The velocity of the convective front is the fluid velocity $\overline{\mathbf{u}}$. The latter is not considered explicitly a DOF of the problem because it can be derived by the Darcy velocity according to Eq. (2). Other parameters are the porosity n, which is considered constant within the fluid step (the variability in time is taken into account in the coupled code as explained later), the fluid density ρ_f, the fluid dynamic viscosity μ, and the body force $\mathbf{b}$. The $\mathbf{D}$ term in Eq. (1) represents the resistance law, i.e., the dissipative effect on the seepage flow caused by the presence of the rockfill. Several different resistance laws are available in the literature for calculating the seepage in rockfill materials (Li 1995). In the present work,

Table 1. Properties of Rockfill Material

Name	Symbol	Value
Porosity	n	0.41
Diameter (mm)	D_{50}	35.04
Dry density (kg/m³)	ρ_s	1,490
Saturated density (kg/m³)	ρ_{sat}	1,910
Apparent specific weight (kg/m³)	W	2,500
Pore index	P_i	0.68
Internal friction angle range (degrees)	ϕ'	37.0−42.5

a nonlinear form of Darcy's law is taken into account, and Ergun's coefficients are chosen for its definition (Larese 2012). In fact, because the objective of the CFD model is to simulate the free surface flow through the rockfill and outside of the same, an essential requirement for the resistance law is that it should automatically go to zero when $n = 1$

$$\mathbf{D} = \frac{\mu}{k}\mathbf{u} + \frac{1.75}{\sqrt{150}} \frac{\rho_f}{\sqrt{k}n^{3/2}}\mathbf{u}^2 \tag{3}$$

where k = permeability that can be calculated as a function of n and D_{50}, which is the diameter of the sieve at which the 50% of the material passes

$$k = \frac{n^3 D_{50}^2}{150(1 - n)^2} \tag{4}$$

The following boundary and initial conditions complete the definition of the fluid problem:

$$\mathbf{u}(\mathbf{x}, 0) = \mathbf{u}_0(\mathbf{x}) \quad \text{in} \quad \Omega$$

$$\mathbf{u}(\mathbf{x}, t) = \mathbf{g}(\mathbf{x}, t) \quad \text{on} \quad \partial\Omega_D, t \in (0, T) \tag{5}$$

$$\mathbf{n} \cdot \boldsymbol{\sigma}(\mathbf{x}, t) = \mathbf{t}(\mathbf{x}, t) \quad \text{on} \quad \partial\Omega_N, t \in (0, T)$$

where $\partial\Omega_D$ and $\partial\Omega_N$ = fluid Dirichlet and Neumann boundaries, respectively.

The weak form of these equations is obtained using a Galerkin discretization. Eq. (1) is solved using a fractional step approach (Codina 2001). Pressure-splitting approaches of the fractional-step type are very convenient because of their high computational efficiency for flows at high R, and they have enjoyed widespread popularity since the original works of Chorin (1967) and Témam (1969). The fundamental idea is to solve the momentum equation by keeping the pressure fixed and later correcting the pressure to guarantee the satisfaction of the divergence constraint.

Traditionally, fractional step algorithms are presented in an implicit context for the time integration of the momentum equation. Nevertheless, in dealing with free surface problems with large distortion of the moving boundaries, the restriction of the time step may be as strict as in the case of an explicit algorithm. For this reason, the authors decided to implement a semiexplicit integration scheme

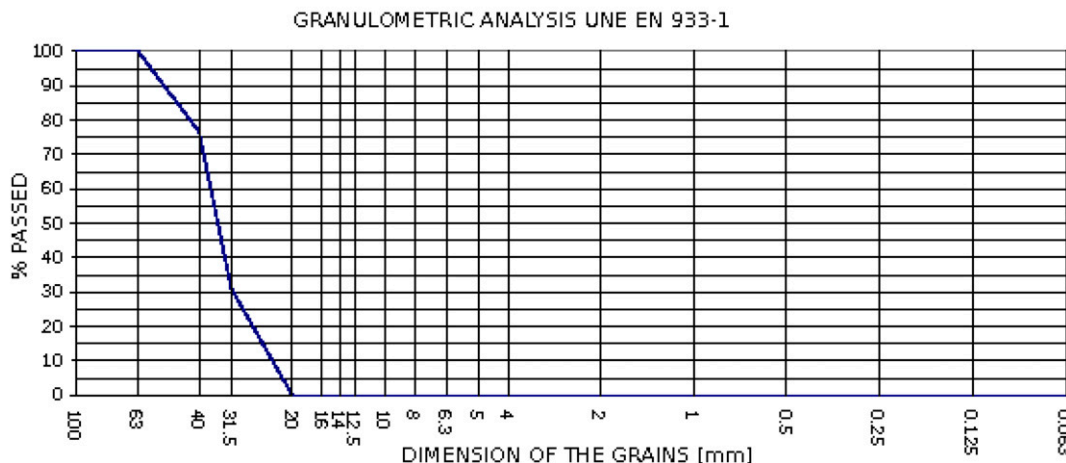| SIEVES UNE	63	40	31.5	20	16	14	12.5	10	8	6.3	5	4	2	1	0.50	0.25	0.125	0.063
% PASSED	100.0	76.6	31.0	0.1	0.1	0.1	0.1	0.1	0.1	0.1	0.1	0.1	0.1	0.1	0.1	0.1	0.1	0.1

Fig. 5. Granulometric curve of rockfill material according to UNE-EN 933-1 [Spanish Association for Standardization and Certification (AENOR) 2012]

© ASCE

Int. J. Geomech.

using a fourth-order Runge-Kutta. Among the Runge-Kutta family method, the fourth order has been proven to be the optimal compromise between the number of intermediate steps and the permissible time step size (Donea and Huerta 2003). Velocity is therefore treated explicitly, whereas pressure remains implicit. The authors assume a linear variation of the pressure within a time step, ensuring the divergence free condition at the end of the step (Larese et al. 2012).

Being a fixed mesh approach, a level set technique is used for tracking the evolution of the free surface. The level set method was conceived as a methodology to following moving interfaces. The moving boundaries (in this case the free surface or seepage line) are composed of the zero-valued isosurface of a given smooth function, which is convected at each time step according to the fluid velocity

field and providing the volume conservation properties (Osher and Fedkiw 2003).

A parallel edge–based solution approach has been implemented to improve the efficiency of the CFD code.

All the implementation details can be found elsewhere (Rossi et al. 2013; Larese et al. 2012; Larese 2012) and are not reported here because this exceeds the scope of the paper.

Dam Structural Response

The structural stability of rockfill slopes is heavily influenced by its interaction with water. Traditionally, the coupled problem of soils or rock and water is tackled by treating the mixture of soil, water, and air as a multiphase material whose behavior is governed by the coupling between the different phases: soil, water, and air. The first mathematical models describing the coupling between the solid linear elastic material and the fluid phase were developed by Biot (1941, 1955). The extension of this work to nonlinear problems with large deformations was carried out by Zienkiewicz and Shiomi (1984). More recently, important steps forward have been made by Lewis and Schrefler (1998), Coussy (1995), and de Boer (2000). An interesting application of the Biot theory using a mesh-free method was recently proposed by Khoshghalb and Khaliki (2010).

Unfortunately, these classical and well-established approaches may not be considered as an alternative in the present work. The main reason for this is the quasi-static nature of such approaches that does not represent the rapidly varying dynamic behavior of seepage
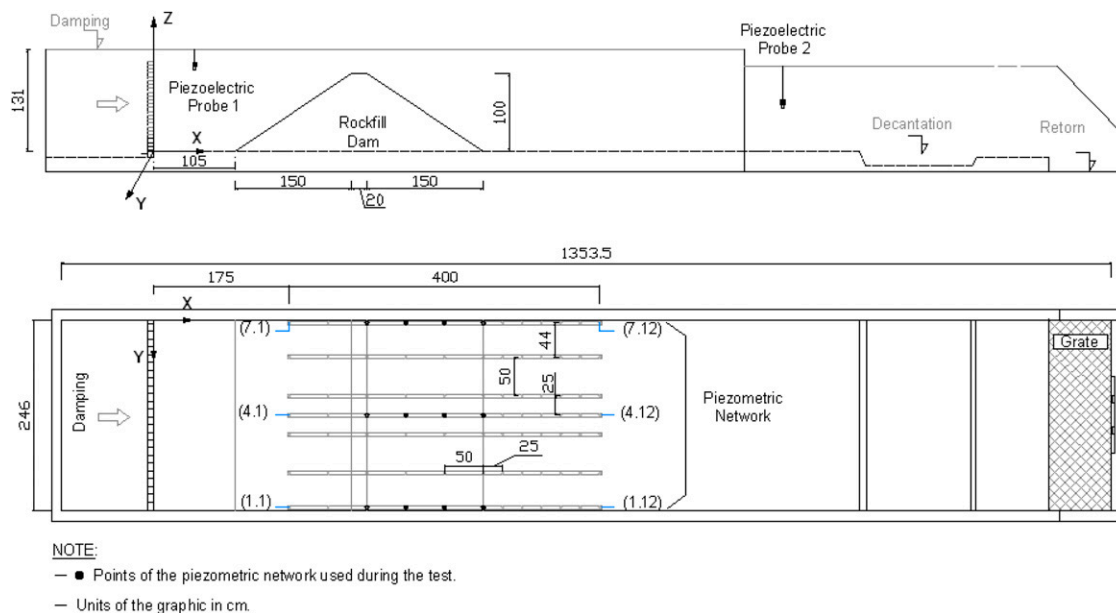
Table 2. Case Studies

Failure status	Case A: homogeneous dam (L/s)	Case B: core dam (L/s)
Without failure	A1 $Q = 25.46$	B1a $Q = 5.93$
		B1b $Q = 4.00$
		B1c $Q = 16.70$
With failure	A2.1 $Q = 51.75$	B2a.1 $Q = 19.36$
	A2.2 $Q = 69.07$	B2a.2 $Q = 30.45$
	A2.3 $Q = 90.68$	B2a.3 $Q = 39.56$

NOTE:
— ● Points of the piezometric network used during the test.

— Units of the graphic in cm.

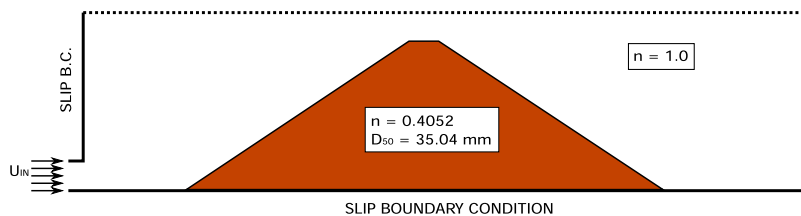**Fig. 6.** Case A: geometry of the experimental setup and map of the sensor distribution

Fig. 7. Case A1: qualitative model geometry and boundary conditions
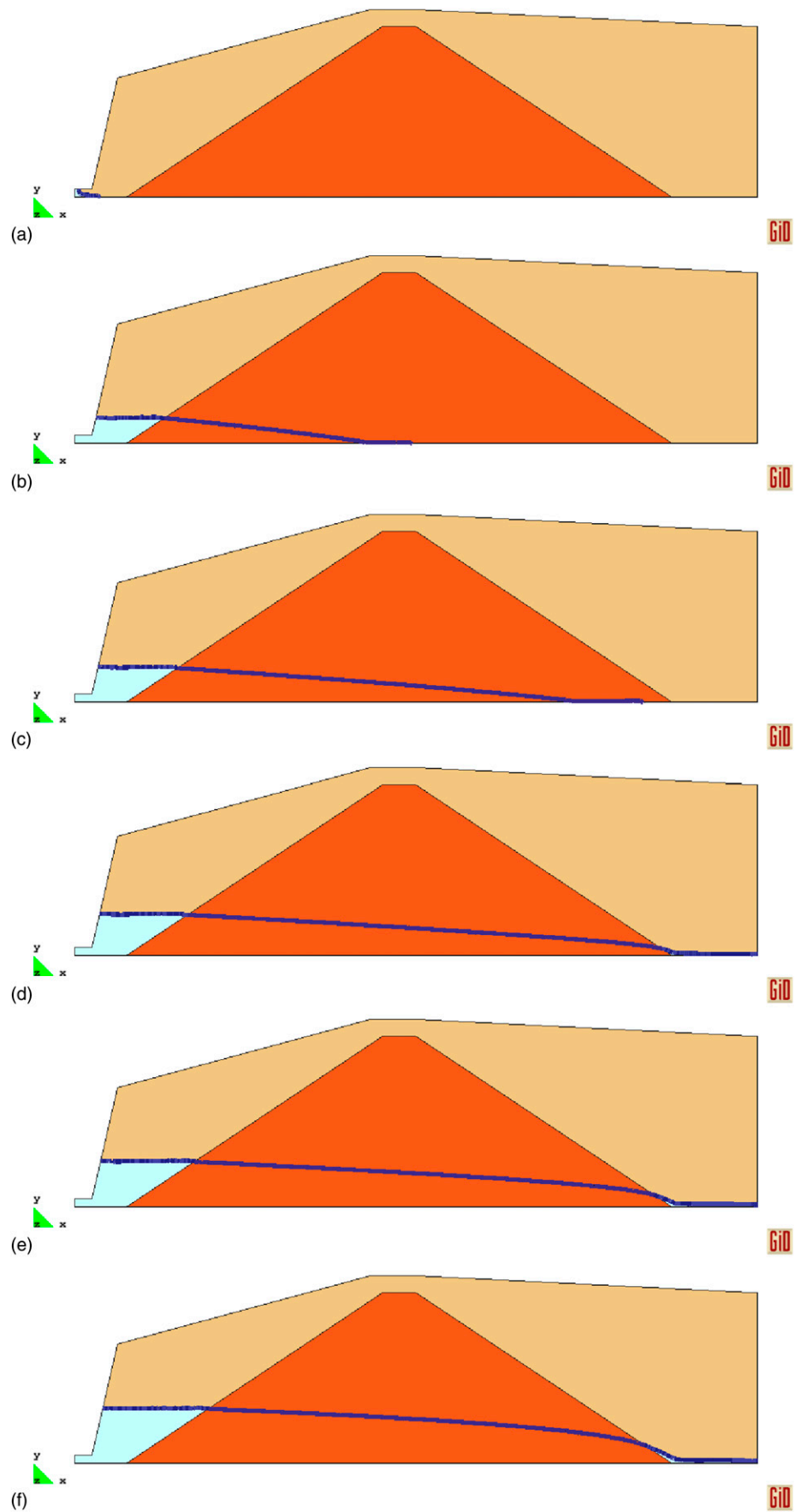
Fig. 8. Case A1: evolution of the seepage line in a dam with porosity $n = 0.41$, $D_{50} = 35.04$ mm, and $Q = 25.46$ L/s: (a) 0.25 s; (b) 10 s; (c) 20 s; (d) 30 s; (e) 40 s; (f) 100 s
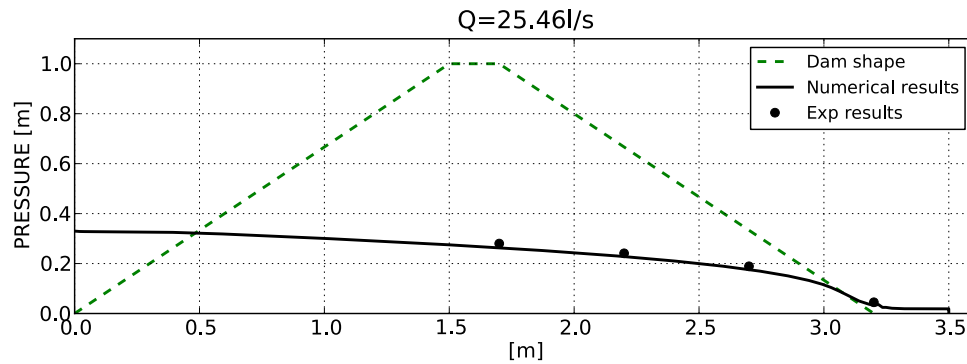
Fig. 9. Case A1: bottom pressure distribution at stationary regime for $Q = 25.46$ L/s, porosity $n = 0.41$, and $D_{50} = 35.04$ mm: numerical and experimental comparison

and rockfill failure, which may happen in overtopping scenarios. Furthermore, for rockfill dams, the problem can always be considered as fully drained as the pores are interconnected, and the effect of the pore pressure is not as dominant as in the classical cases. This in turn allows us to neglect the computation of the saturation level and the interaction between air and water in the matrix.

It is important to remark that these considerations are valid for the rockfill layers of a dam. A different problem is the simulation of the structural response of the clay core. This problem is out of the scope of the present paper. In fact, as explained in the introduction, the aim of the paper is to simulate the onset and evolution of the breaches by considering the clay core intact.

Several depth-integrated models have recently been developed for simulating dam breach formation (Wang and Bowles 2006; Faeh 2007; Froehlich 2008). These algorithms evaluate the erosion effect on embankments using sediment transport algorithms more than studying the failure mechanism. In some cases, seepage is not even considered, and just the breaching caused by superficial dragging is calculated.

Given that the time scale of the exceptional flooding can be of the order of minutes to hours, the dam material can be considered as rigid (avoiding any elastic response in the unyielded region), and its compressibility can be neglected. In fact, the volume of the porous matrix is not significantly modified during an exceptional flooding, and the compressibility of a single grain is negligible in comparison with the large deformations to which it may be subjected.

Finally, the tracking of the material yield surface is not crucial because the elastic recoverable strains induced by the transient phenomena are negligible.

The adoption of a continuous approach for the dam body leads to an additional requirement: the choice of a suitable constitutive law (Varadarajan et al. 2006). Many plastic or rigid-plastic constitutive models are commonly used in geomechanics to describe the structural response of an incoherent noncohesive material, but in most cases, the long-term behavior is analyzed (Dolezalova and Hladik 2011).

It is usually accepted that a rockfill slope has the capability to support a certain amount of shear stress with almost no elastic strains before starting to suffer large deformations. When the yield stress is reached, the material starts to flow until a new stable configuration is achieved. Under such conditions, the behavior of the yielded material is more similar to the flowing of a fluid than to the deformation of a solid. Taking this consideration into account, a variable-viscosity model seems adequate for this type of material behavior. This model is simpler to implement than classical plastic models but is still able to capture the essence of the complex material

Table 3. Case A1: Mesh Sizes Used in the Mesh Sensitivity Study

Parameter	Mesh A	Mesh B	Mesh C	Mesh D
Dimension (m)	0.01	0.10	0.15	0.20
Number of elements	43,500	550	310	220
Number of nodes	86,100	970	510	340

deformation phenomena. A wide category of fluids exhibit a rigid behavior until reaching a yield threshold. They are part of the family of the so-called non-Newtonian fluids. In the present work, a non-Newtonian constitutive law for simulating the rockfill material is used. This implies that the rockfill stiffness is controlled by very high values of the so-called apparent viscosity $\tilde{\mu}_s$, which is, by definition, the ratio between the shear stress and the shear rate. Only when the yield threshold is exceeded does the apparent viscosity decrease and the material start flowing. When the material stops its motion, $\tilde{\mu}_s$ recovers its initial value for which the stress level does not exceed the yield limit.

The model chosen in this work has its origin in the traditional modeling of Bingham plastics using the regularization proposed by Papanastasiou (1987). However, to include a Mohr-Coulomb failure criteria (with no cohesion), the possibility of considering a variable yield level is introduced (Larese 2012). The yield stress is calculated as $\tau_0 = p'_s tg(\phi')$, where p'_s is the effective pressure, and ϕ' is the internal friction angle that depends on the effective pressure (this means that the pore pressure is subtracted by the results of the triaxial test performed).

Considering all the previous assumptions, the Bingham regularized relation is

$$\boldsymbol{\tau}_s = 2 \left[\mu_s + \frac{p'_s tg(\phi')}{\dot{\gamma}} \left(1 - e^{-m\dot{\gamma}} \right) \right] \boldsymbol{\varepsilon}_s(\mathbf{u}_s) \qquad (6)$$

where μ_s = fluidized viscosity; m = regularization parameter that controls the approximation to the bilinear model; and $\dot{\gamma}$ = equivalent strain rate defined as the second invariant of the rate of strain tensor $(\boldsymbol{\varepsilon}_s)$ $\dot{\gamma} = [(1/2)\boldsymbol{\varepsilon}_s{:}\boldsymbol{\varepsilon}_s]^{1/2}$.

The apparent viscosity $\tilde{\mu}_s$ is defined as

$$\tilde{\mu}_s(\dot{\gamma}) = \mu_s + \frac{p'_s tg(\phi')}{\dot{\gamma}} \left(1 - e^{-m\dot{\gamma}} \right) \qquad (7)$$

The governing equations for the structural problem are written as (Larese et al. 2012)
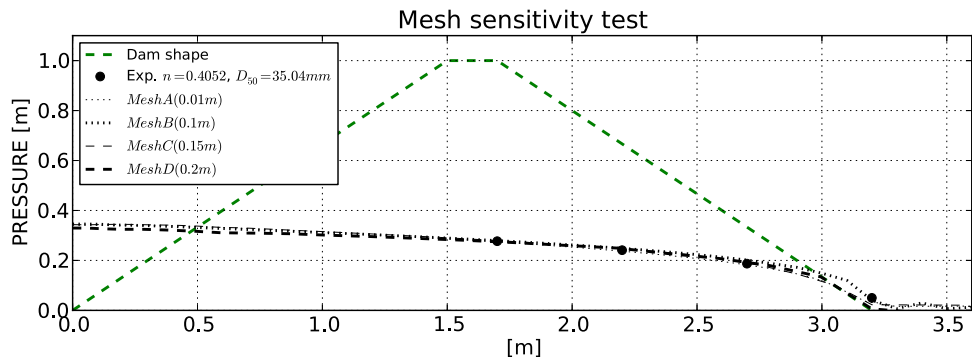
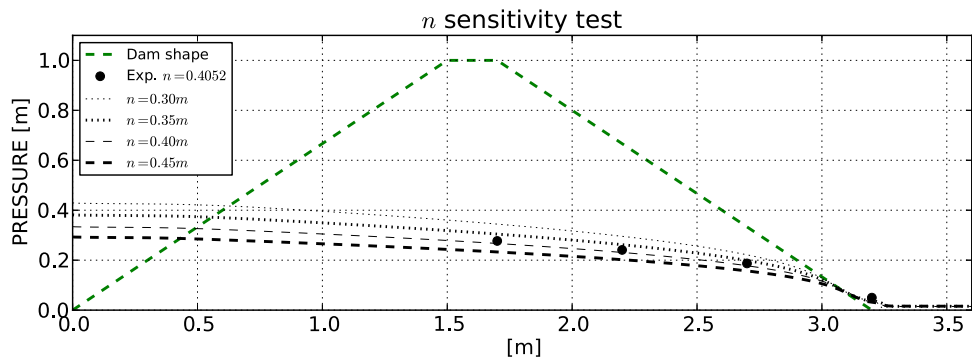**Fig. 10.** Case A1: influence of the mesh

Fig. 11. Case A1: pressure head distribution for porosity $n = 0.3, 0.35, 0.4,$ and 0.45
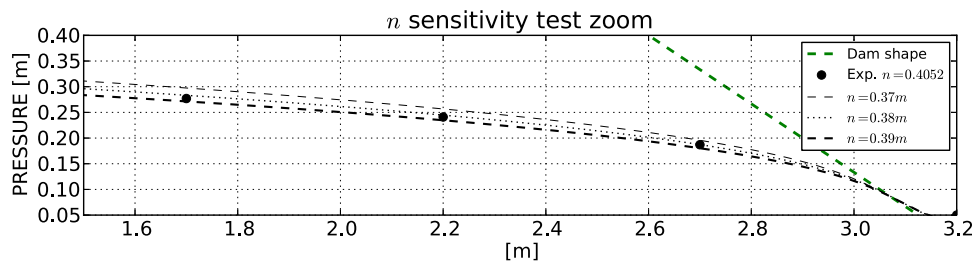

Fig. 12. Case A1: zoom of the pressure head distribution for porosity $n = 0.37, 0.38,$ and 0.39
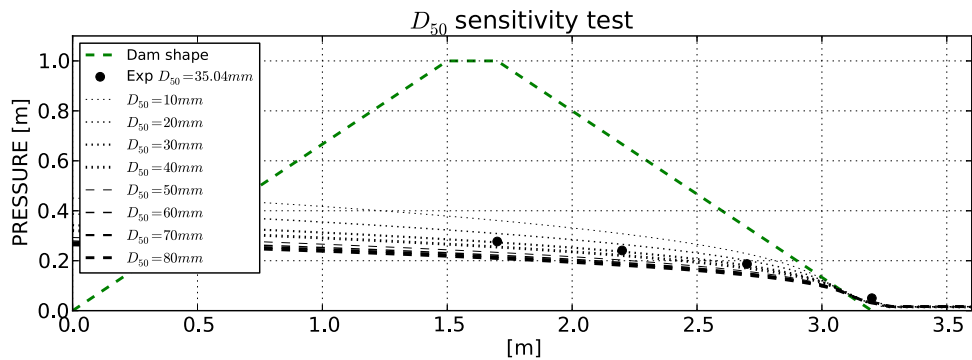

Fig. 13. Case A1: influence of the diameter of the material

$$\rho_s \partial_t \mathbf{u}_s + \rho_s \mathbf{u}_s \cdot \nabla^s \mathbf{u}_s + \nabla p_s' - 2\nabla \cdot \tilde{\mu}_s \nabla \mathbf{u}_s - \rho_s \mathbf{b}_s$$
$$+ (1-n)\nabla p - \mathbf{D} = 0 \quad \text{in} \quad \Omega_s, \ t \in (0,T) \quad (8)$$
$$\nabla \cdot \mathbf{u}_s = 0 \quad \text{in} \quad \Omega_s, \ t \in (0,T)$$

where the DOFs of the problem are the effective pressure (p_s') and the solid velocity (u_s); ρ_s = rockfill density; $\mathbf{b}_s$ = vector of body forces; and p and $\mathbf{D}$ = fluid pressure and resistance law terms defined in Eqs. (1) and (3), respectively. The resistance law term $\mathbf{D}$ and the gradient of fluid pressure $[(1-n)\nabla p]$ act as external forces in the structural problem. This is correct under the assumption that during the deformation process, the fluid velocity can be considered larger than the structural one, and therefore, $\mathbf{D}$ can be expressed in terms of the fluid velocity only. Note that in the more general form, it should be function of the relative velocity between fluid and rockfill (Larese et al. 2012).

The problem is fully defined with the following boundary and initial condition:

$$\mathbf{u}_s(\mathbf{x},0) = \mathbf{u}_{s0}(\mathbf{x}) \quad \text{in} \quad \Omega_s$$
$$\mathbf{u}_s(\mathbf{x},t) = \mathbf{g}_s(\mathbf{x},t) \quad \text{on} \quad \partial\Omega_{sD}, \ t \in (0,T) \quad (9)$$
$$\mathbf{n} \cdot \boldsymbol{\sigma}_s(\mathbf{x},t) = \mathbf{t}_s(\mathbf{x},t) \quad \text{on} \quad \partial\Omega_{sN}, \ t \in (0,T)$$

where $\partial\Omega_{sD}$ and $\partial\Omega_{sN}$ = structural Dirichlet and Neumann boundaries, respectively.

The PFEM is the numerical technique used for solving the equations simulating the dam failure process (Larese et al. 2008). In the PFEM, the domain is modeled via an updated Lagrangian formulation. All the variables are assumed to be known at the current configuration at time t, and they are brought to the next (or updated) configuration at time $t + dt$. The FEM is used to solve the continuum mechanics equations in a mesh built up from the underlying nodes. This is useful to model the separation of solid particles from the solid surfaces interacting with the fluid and to follow their subsequent motion as individual particles with a known density, an initial acceleration, and a velocity subjected to gravity forces (Oñate et al. 2004; Idelsohn et al. 2004).

Table 4. Activated Sensors Lines in Case A

Line	Y-coordinate (m)
1	0.04
4	1.23
7	2.42

It is important to remark that in PFEM, each particle is treated as a material point characterized by the density of the solid domain to which it belongs, and the global mass is obtained by integrating the density at the different material points over the domain. The quality of the numerical solution depends on the discretization chosen as in the standard FEM, and adaptive mesh refinement techniques can be used to improve the solution in zones where large gradients of the fluid or the structure variables occur.

Early applications of PFEM focused on the simulation of free surface flows and breaking waves (Idelsohn et al. 2004). Since those days, PFEM has been successfully used in a wide range of fields such as fluid-structure interaction (FSI) and coupled problems (Oñate et al. 2011a, b; Ryzhakov et al. 2010), multifluid problems (Mier et al. 2011), contact problems and geotechnical simulations (Carbonell et al. 2010; Oñate et al. 2008), and fire engineering (Butler et al. 2007; Marti et al. 2012). The PFEM has also been successfully used in the implementation of Bingham plastics model for the simulation of landslides (Salazar et al. 2012; Cremonesi et al. 2011).

The basic ingredients of PFEM for solving a FSI problem can be summarized as follows:
- An updated Lagrangian kinematic description of motion of the points in the fluid and solid domains;
- A boundary recognition method (α-shape);
- A fast remeshing algorithm; and
- Use of the FEM for the solution of the governing equations.

In the present work, an implicit algorithm has been implemented for the FEM solution, using a monolithic strategy to solve the governing equations and a Bossak time integration scheme (Larese 2012).

Coupling Strategy

The use of a staggered explicit scheme is highly favored when using different kinematic frameworks for the fluid and dam problems. Moreover, this is a natural choice to take advantage of the implicit structural solver that allows bigger time steps than the explicit CFD (the ratio is typically 10 fluid steps per structural step).

The variables of the structural Lagrangian model are projected onto the Eulerian fixed mesh where, at the beginning of the simulation, the only available information is the incoming discharge of water and the control domain. The idea is that the fluid analysis step is evaluated once the distribution of porosity is projected from the structural domain. Once the fluid problem is solved, the relevant variables are, in turn, projected onto the Lagrangian structural mesh.
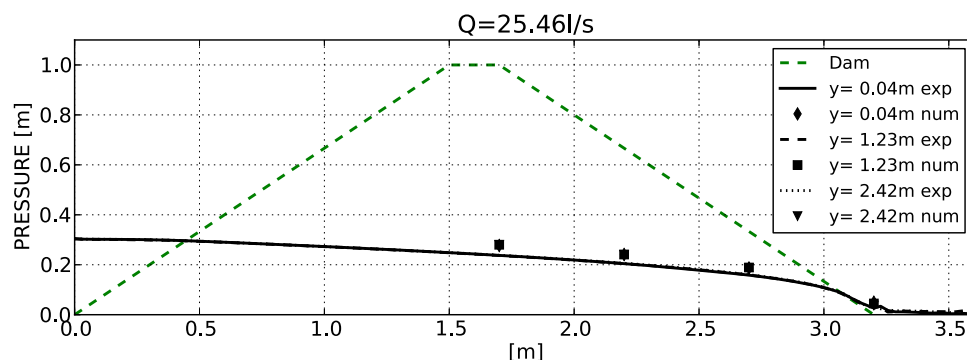

Fig. 14. Case A1 (3D): bottom pressure distribution at stationary regime along the three sensors lines ($Y = 0.04, 1.23,$ and 2.42 m, respectively) for $Q = 25.46$ L/s, porosity $n = 0.41$, and $D_{50} = 35.04$ mm: numerical and experimental comparisons

---

© ASCE

04014060-9

Int. J. Geomech.

These variables include the fluid pressure and the Darcy forces to evaluate correctly the external force term of the structural momentum [Eq. (8)]. Once this is done, the structural response of the dam can be calculated. The rockfill material and consequently the Lagrangian mesh deforms according to the velocity and pressure fields obtained in the structural analysis step. To avoid inverted elements, the mesh is regenerated at the end of the step. The deformed rockfill domain is then projected onto the Eulerian mesh to solve for the subsequent time step, and so on.

The key steps of the FSI analysis process are shown in Fig. 1. The flowchart of the algorithm is schematically subsequently summarized.
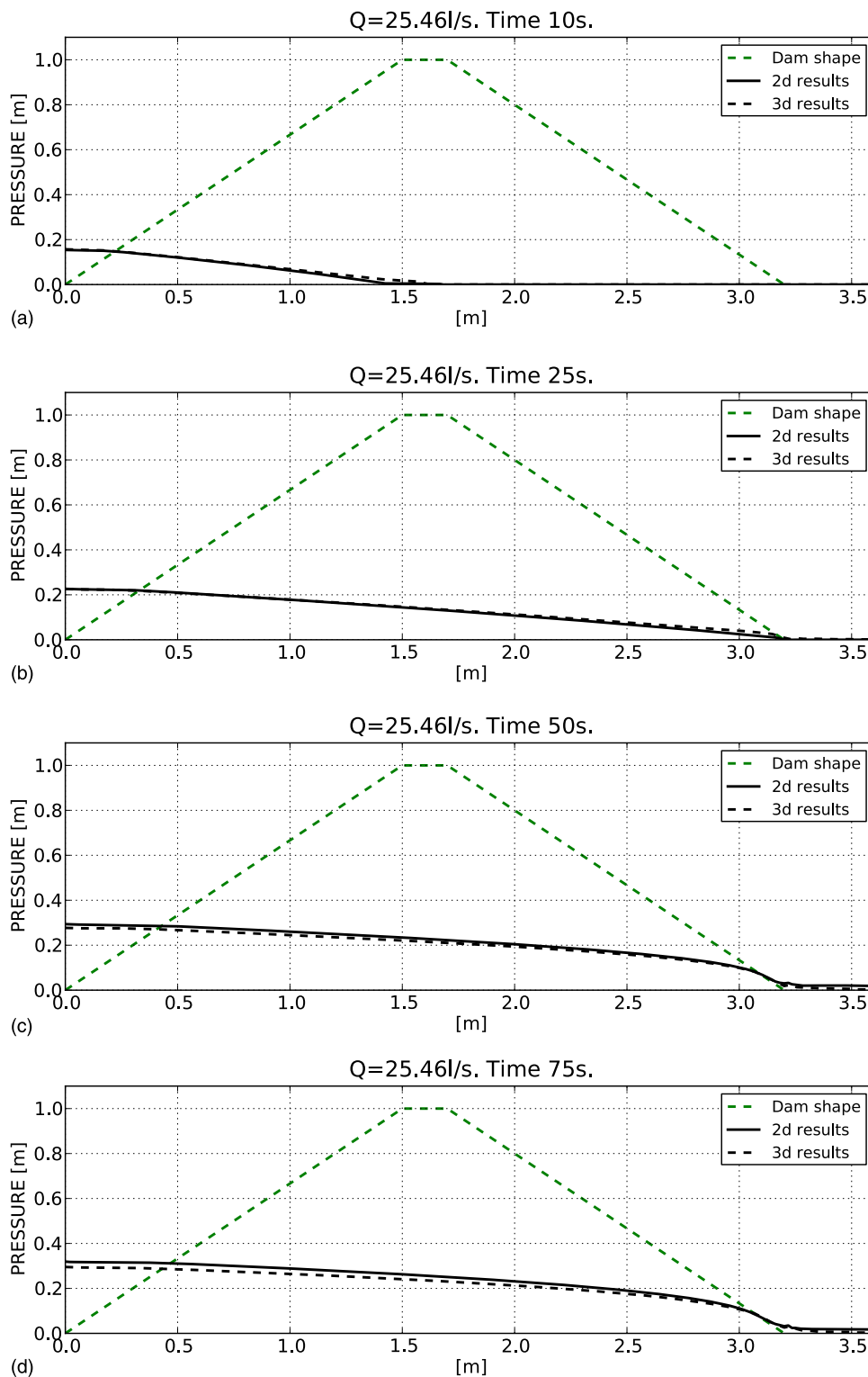

Fig. 15. Case A1: bottom pressure distribution in 2D and 3D models at different instances of the transitory regime ($Q = 25.46$ L/s, porosity $n = 0.41$, and $D_{50} = 35.04$ mm): (a) 10 s; (b) 25 s; (c) 50 s; (d) 75 s

---

Assuming the solution of the coupled problem to be known at time step t^n. The solution at $t^{n+1} = t^n + dt_s$ (dt_s is the time increment of the implicit structural solver and dt_f is the fluid one) is obtained by providing the following steps:

1. Project the configuration of the rockfill material in terms of the porosity distribution on the Eulerian fluid domain;
2. While $t_f^{n+1} \leq t^{n+1}$ (where $t_f^{n+1} = t^n + dt_f$), solve the water free-surface flow problem calculating the velocity and pressure field in an Eulerian fixed mesh;
3. Project the fluid velocity and pressure fields on the Lagrangian structural mesh;
4. Project the nonlinear Darcy term on the Lagrangian structural mesh;
5. Calculate the structural response of the rockfill material in the Lagrangian mesh using PFEM; and
6. Go back to Step 1.

Model Validation: Numerical versus Experimental Results

As a first step in the validation of the fluid flow and coupled FSI codes, the authors numerically reproduced a set of experiments performed at the Technical University of Madrid (UPM) [XPRES project "Development of a Method for Studying the Failure Process of Rockfill Embankment Dams Combining Finite Element and Particle Techniques" (National Plan R+D of the Spanish Ministry of Science and Innovation I+D, BIA2007-68120-CO3-01); and E-DAMS project "Numerical and Experimental Techniques for Safety Assessment and Protection of Embankment Dams in Over-topping Scenarios" (National Plan R+D of the Spanish Ministry of Science and Innovation I+D, BIA2010-21350-C03-00)]. The main objective of the experiments was the analysis of the influence of a series of parameters and of their combination on the failure mechanism of the dam. Each experiment studied a physical model of a dam under a series of incremental steps of discharge. After each increment, the incoming discharge was kept constant until the steady state was reached.

Pressure heads were registered, and the advance of failure was measured at each analysis step. Pressure at the bottom of the flumes was evaluated by a network of sensors [Fig. 2(a)], and its value was read on millimetric panels [Fig. 2(b)].

The dam deformation was analyzed through the evolution of the so-called advance of failure (termed as B in the following). This is, by definition, the horizontal projection of the distance between the initial undeformed downstream toe and the higher point of the failed area (Toledo et al. 2004). Usually colored horizontal strikes were painted on the slope. This helps the measurement of B [Fig. 3(b)]. In some of the experiments, a more detailed measurement of the evolution of failure was performed using a close object photogrammetry technique. This consists of taking a series of pictures with a very short time interval until
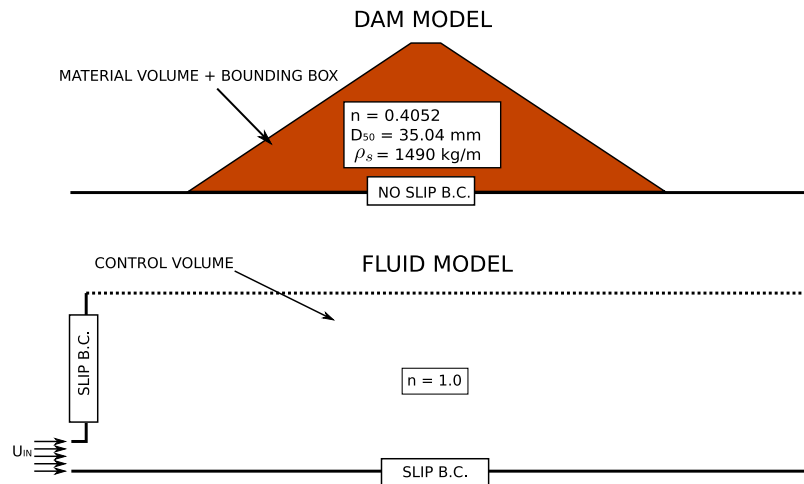

Fig. 16. Case A2: coupled model; fluid and dam geometry and boundary conditions (Springer and Computational Mechanics, vol. 50, 2012, pp. 805–819, "A coupled PFEM-Eulerian approach for the solution of porous FSI problems," Larese, A., Rossi, R., Oñate, E., and Idelsohn, S. © *Computational Mechanics*, with kind permission from Springer Science and Business Media)
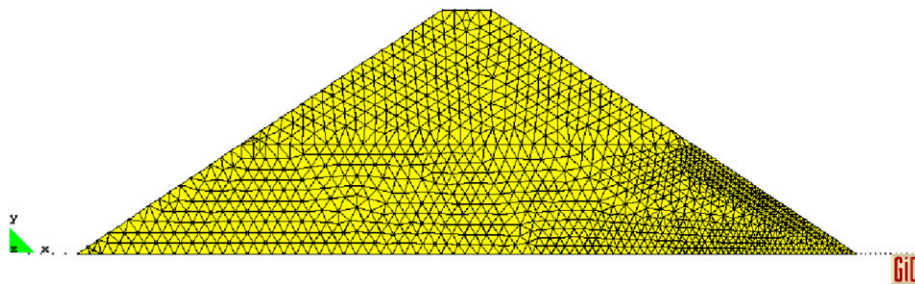

Fig. 17. Case A2: 2D mesh of the dam model; 3,400 linear triangular elements
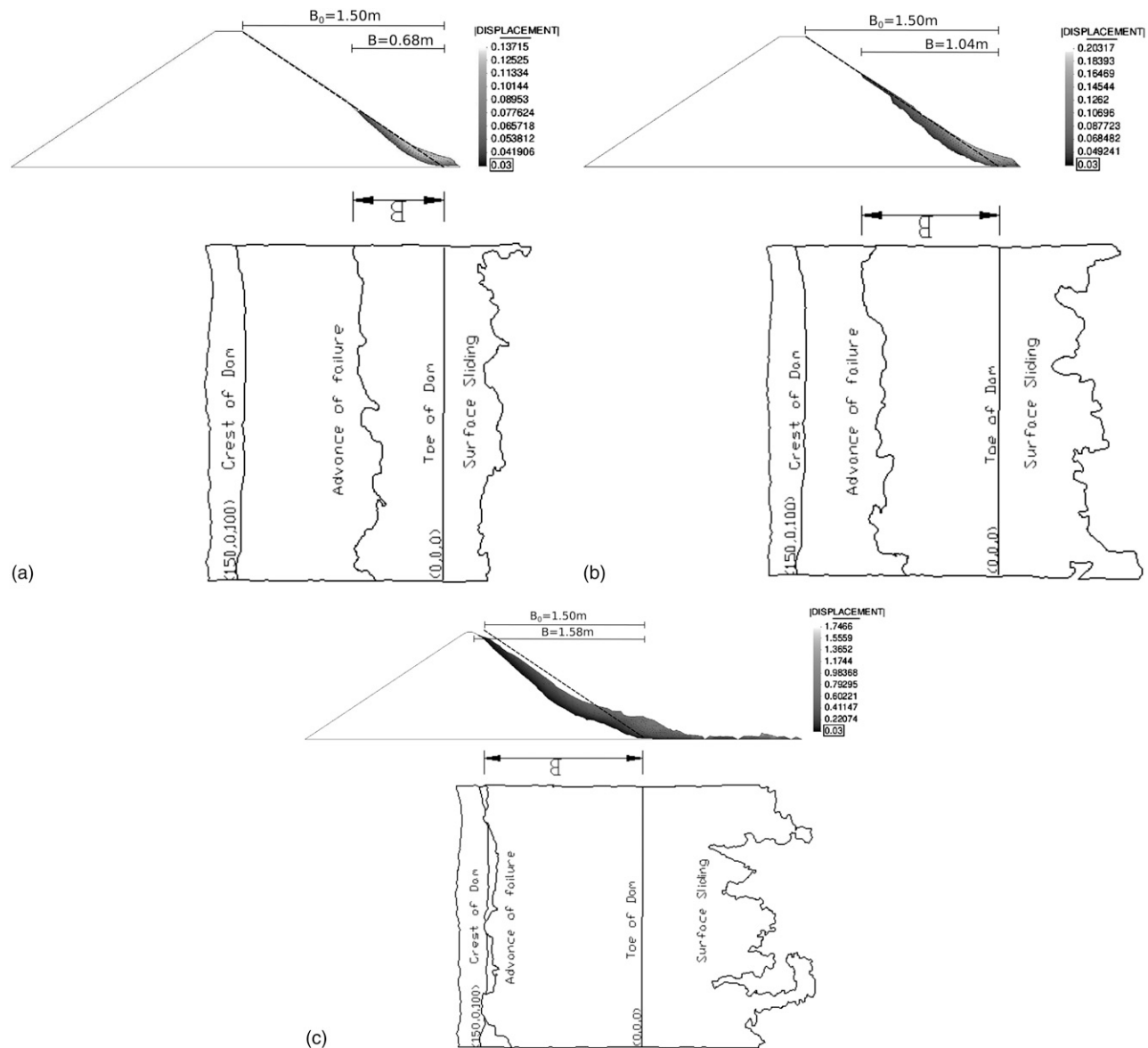
Fig. 18. Advances of failure for different inflow discharges: comparison between experimental and numerical results; contour fill of numerical displacement > 3 cm and digital model of the deformed slope in the experiments (plant view of the downstream shoulder): (a) $Q_2 = 51.75$ L/s; (b) $Q_3 = 69.07$ L/s; (c) $Q_4 = 90.68$ L/s (Springer and Computational Mechanics, vol. 50, 2012, pp. 805–819, "A coupled PFEM-Eulerian approach for the solution of porous FSI problems," Larese, A., Rossi, R., Oñate, E., and Idelsohn, S. © *Computational Mechanics*, with kind permission from Springer Science and Business Media)

the end of the simulation. Through the processing of these data, a digital model of the deformed dam was created and the dynamic evolution of the breach was followed with higher precision (Fig. 4). The experiment ended when failure reached the crest of the dam.

The collapse settlement of the rockfill caused by wetting at the first saturation was not considered because such a phenomenon manifests after the drawdown of the water level inside the shoulder, which is when the failure has already occurred.

The analysis of the experimental campaign is not the objective of the present work and has been previously described (Larese et al. 2010; Lechuga et al. 2010; Campos et al. 2010; Morán and Toledo 2011).

The evolution of seepage and beginning of failure in two different types of dams were simulated: a homogeneous dam, without any sort of impermeabilization, and a core dam.

Table 5. Case A2: Comparison between Experimental (B_{exp}) and Numerical (B_{num}) Advance of Failure

Case	Q (L/s)	B_{exp}	B_{num}	Error (%)
A2.1	51.75	0.71	0.68	4.2
A2.2	69.07	1.08	1.04	3.7
A2.3	90.68	1.56	1.58	1.3

The objective was to prove the reliability of the code when simulating rockfill in the overtopping condition, and for this purpose, flow-through structures and not real dams were used for the study of seepage. This allow concentration on a single phenomenon, which is essential for the validation of the code, and easy repetition of the experiment to prove the accuracy of the results.
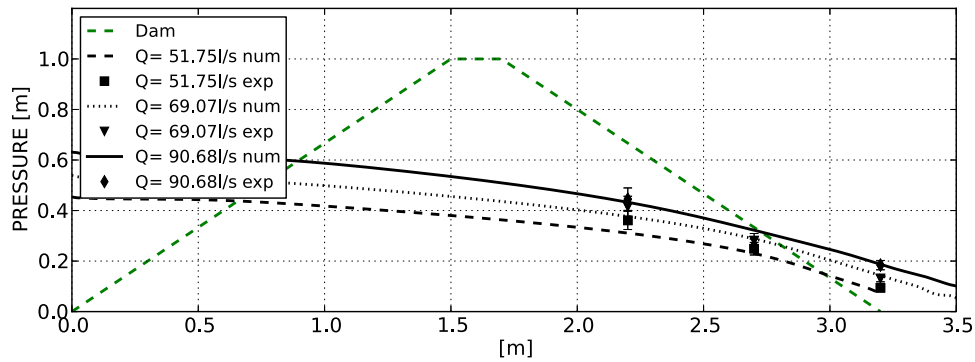
Fig. 19. Bottom pressure distribution at stationary regime for different discharges (porosity $n = 0.41$, $D_{50} = 35.04$ mm): numerical and experimental comparison
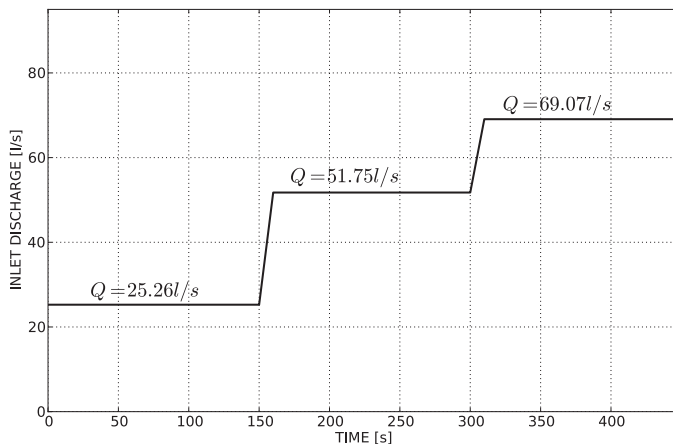

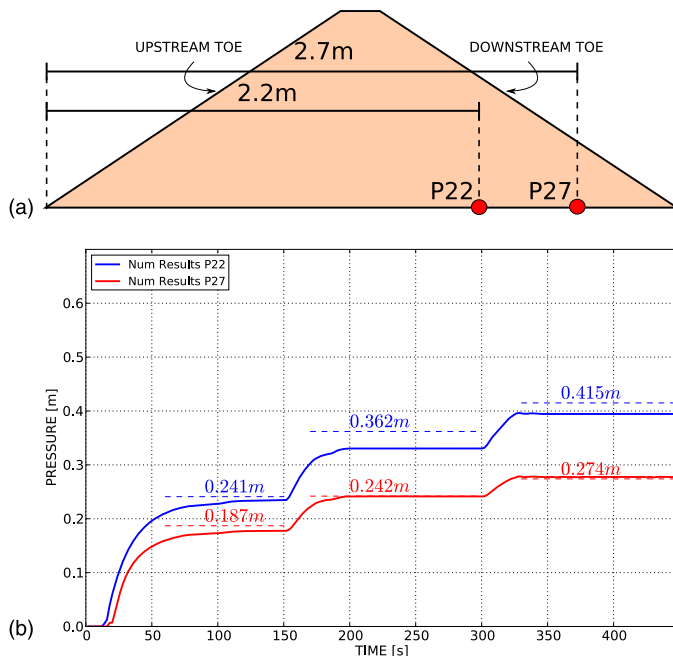**Fig. 20.** Imposed incoming discharge in function of time

Fig. 21. Bottom pressure distribution considering the hydrograph presented in Fig. 20 (porosity $n = 0.41$, $D_{50} = 35.04$ mm): numerical and experimental comparison: (a) sensors position; (b) pressure evolution on the sensors

Conversely, the numerical models always reproduce the experiments at the same scale; this implies that no similarity criterion was needed.

All the dams considered have the same downstream slope: 1.5*H*:1*V*, which is a common ratio in real dams. This geometrical aspect strongly determines the deformation of the rockfill. Experimental evidence shows that mass sliding is predominant in this kind of slopes. The coupled code has been conceived for representing the predominance of this failure mode. For flat slopes (i.e., 3*H*:1*V*), less frequent in practice, the inclusion of an algorithm to simulate dragging of surface particles is required.

Only one material was analyzed, and its characteristics were obtained by an external laboratory according to Spanish norms. These are summarized in Table 1. The rock chosen is limestone, and the rockfill used is quarry stone. The granulometric distribution, according to UNE-EN 933-1 [Spanish Association for Standardization and Certification (AENOR) 2012], is the one shown in Fig. 5. The diameter for which the 50% of the material passes the sieves (D_{50}) is 35.04 mm, and porosity is 0.41 (lower than the pore index, which is the ratio between the empty and the solid volume). The material used is not well grained but quite uniform, which negates the influence of that parameter. Uniform materials are more porous, and this helps to reproduce R similar to those that can be obtained in larger prototypes with well-grained higher material.

Different steps of discharge were simulated for each experiment. In all cases with the lower discharge considered, no movements in the downstream slope were experimentally observed. This implies that, to speed up the calculations, the fluid uncoupled code can be used for the simulation. The coupled FSI model is used for the higher discharges.

Case Study

Results for two different dams are presented in this work. Before the presentation of the numerical tests, the nomenclature used to classify the case studies is summarized: Case A, a homogeneous dam without impervious elements; Case B, a dam with an internal core. Only the downstream slope is simulated.

For each case *i* (*i* = *A* or *B*), two substep analyses were carried out:
- Case *i*1: Analysis of the nonlinear seepage given an incoming/overtopping discharge. Experimentally, no deformation is observed in the dam body. This analysis is carried out just with the fluid uncoupled code.
- Case *i*2: Analysis of the evolution of failure given an incoming/overtopping discharge. Several increasing values of discharges

are considered for each case according to experiments. In this case, the coupled FSI code is used.

Finally, in Table 2, the discharge (Q in liters per second) for every studied case is detailed.

The position of the pressure sensors and the experimental data for each case are not reported here but can be found in Larese et al. (2011b). This benchmark was selected as part of the XI Benchmark workshop of ICOLD on Numerical Analysis of Dams held in Valencia, Spain, in October 2011. The solution to this benchmark can be found in Larese et al. (2011a).

Case A: Homogeneous Dam

The first example reproduces an experiment carried out at UPM for a dam without any internal core or impervious upstream face. This case is obviously not representative of a real rockfill dam, which cannot be conceived without any impervious element. Nevertheless, it is important to remark that the objective of this study is to provide a numerical technique able to simulate the rockfill failure, and it is important to get a deeper knowledge of the seepage evolution inside an homogeneous medium both for the physical and numerical point of view as a preliminary step to face the complete failure of a real dam.

Case A: Experimental Setup and Geometry

The geometry of the dam model is presented in Fig. 6, where the distribution of all the bottom pressure sensors is shown. Not all the sensors were activated during the experiment but only those under the downstream shoulder of the dam as explained in Larese et al. (2011b).

Case A1: Two-Dimensional Numerical Model and Results

The numerical model is built following the geometry of the experiment (Larese et al. 2011b). The control volume of the Eulerian fluid model has to be large enough to not influence the solution. Concerning the boundary conditions, these are shown in Fig. 7: an inlet with fixed velocity is set in the left side of the control volume (the arrows in the image are indicating the entrance of water). A slip boundary condition is imposed on the bottom and left wall (continuous line in the image), whereas an outlet condition (zero pressure) is imposed on the upper and right side of the domain as shown (dotted line in the image).

The fluid code simulates the filling of the upstream reservoir in the unsteady regime [Figs. 8(a–f) show consecutive time instances of the transient regime] even if experimental data only refer to the steady state. Fig. 9 shows the comparison between the numerical and experimental head of pressure. The agreement is good even if the numerical code slightly underestimates the experimental values. This aspect is more evident in the following examples.
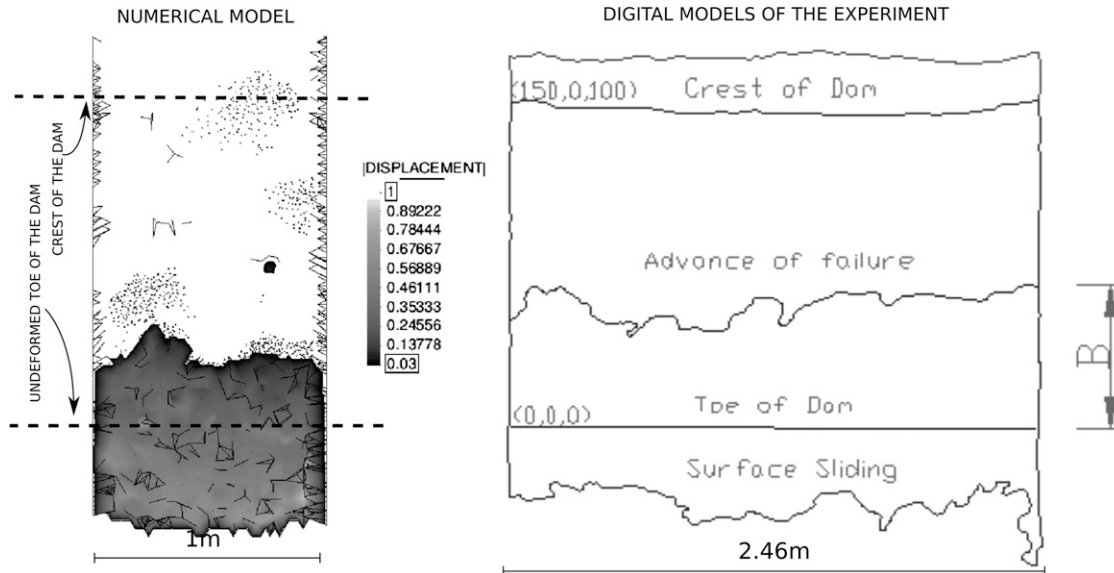

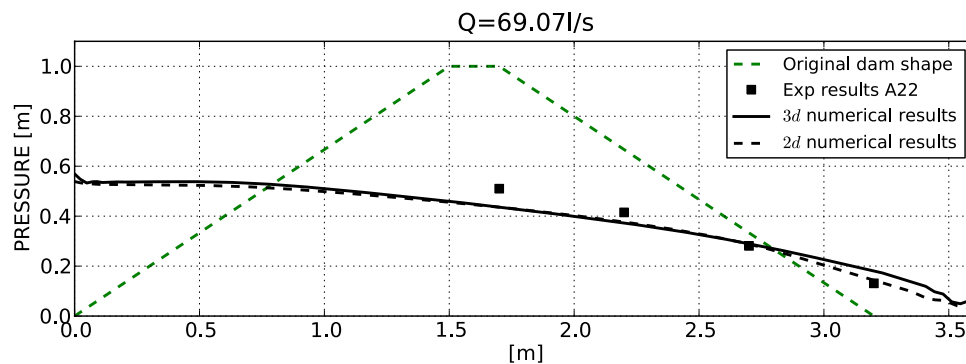**Fig. 22.** Case A2.2 (3D): numerical and experimental advance of failure

Fig. 23. Case A2.2 (3D): bottom pressure distribution at stationary regime for $Q = 69.07$ L/s, porosity $n = 0.41$, $D_{50} = 35.04$ mm: 2D and 3D numerical results compared with experimental data points
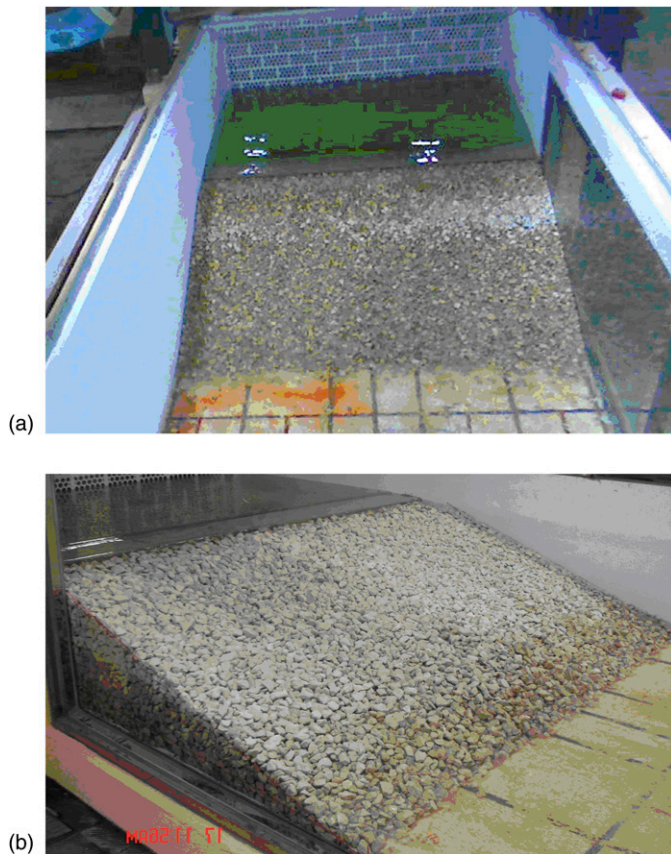
(a)

(b)

Fig. 24. Core dam; experimental setup: (a) upper view; (b) side view (images by authors)

Assuming that the geometry of the experiment and the inflow discharge are correct, the parameters that might influence the results of the model are (1) the quality of the mesh, (2) the value of the porosity n, and (3) the D_{50} value of the rockfill particles.

To understand how an error in the determination of each of these parameters can influence the solution, a deeper analysis is carried out in the following sections.

Case A1: Mesh Influence

Case A1 is run with different meshes to understand how the mesh influences the results. The inlet area has been constantly refined (with $h_{ref} = 0.01$ m, where h is the average mesh dimension and h_{ref} is the refined area at the inlet) to ensure a constant incoming discharge before entering the porous medium. The characteristics of the meshes are summarized in Table 3.

Fig. 10 shows that the mesh does not have a strong influence on the quality of the results, at least inside the dam if no impervious structures are present. The main difference can be observed at the downstream toe of the dam, where water comes out of the granular material. For coarser meshes, an important loss of volume can be observed outside the rockfill. The presence of the porous medium with its dissipative effect is helpful for enforcing the volume conservation properties for very coarse meshes (i.e., Mesh D). This is no longer true outside the granular material.

Case A1: Influence of Porosity

The porosity of the material used in the experiments was evaluated by an external laboratory according to Spanish norm UNE-EN 1936 (AENOR 2007). The porosity value is $n = 0.41$.

Keeping all the parameters of the models and the calculation mesh fixed, porosity is changed in the range of $0.30-0.45$ to see the influence of this parameter on the results. Fig. 11 shows that uniform variation in the porosity induces a uniform increment in the pressure head distribution.

The numerical results obtained for $n = 0.41$ yield a lower pressure head, whereas for $n = 0.35$, they overestimate the experimental data. The same problem was analyzed in more detail considering a smaller
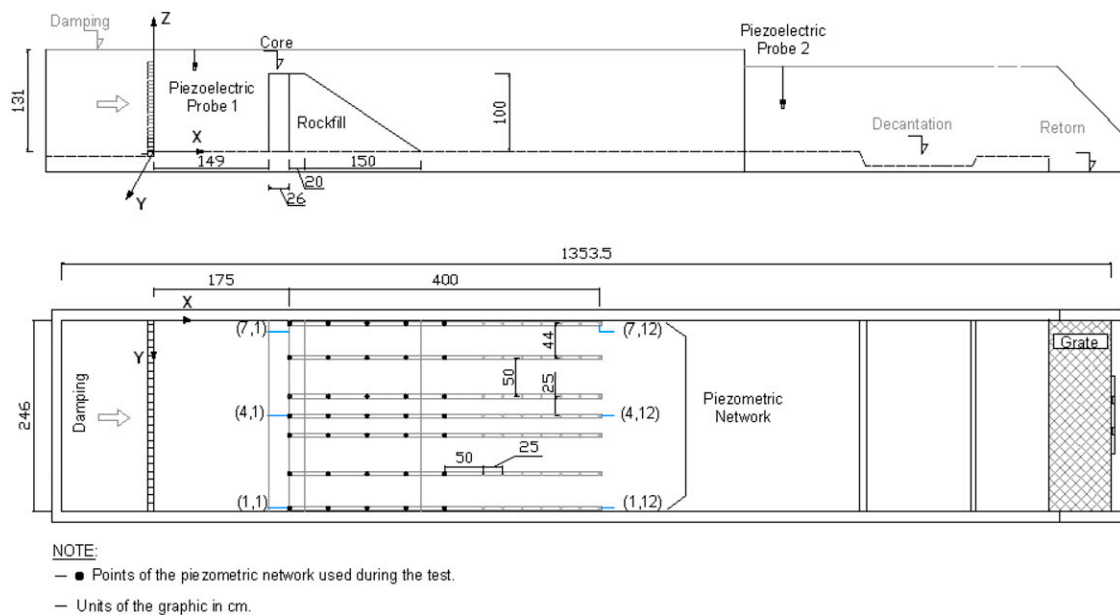

Fig. 25. Case B: geometry of the experimental setup and map of the sensors distribution

porosity increment. The results for $n = 0.37$, 0.38, and 0.39 are shown in Fig. 12. The experimental data agree with the results for $n = 0.38$.

Case A1: Influence of the Diameter of the Material

The last analysis concerns the influence of the D_{50} value. This number is changed with an increment of 1 cm from 1 to 8 cm. Fig. 13 shows that the pressure head is not linear with D_{50}. Thus, for $D_{50} > 5$ cm, its influence on the pressure distribution is negligible. Conversely, the smaller D_{50} is, the larger its influence on the pressure distribution.

Case A1: Three-Dimensional Numerical Model and Results

The three-dimensional (3D) model of Case A was studied using the geometry shown in Fig. 7. The control volume is meshed with 1,264,015 four-noded tetrahedra.
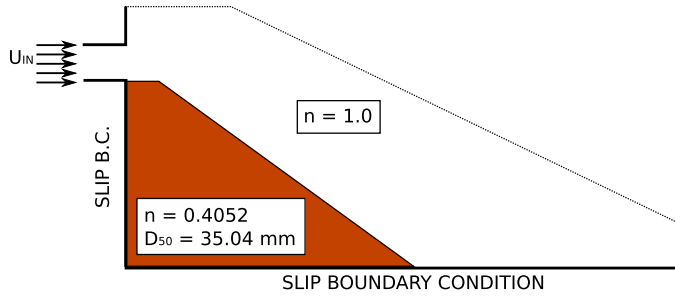

Fig. 26. Case B1: qualitative model geometry and boundary conditions

Three lines of pressure sensors were activated during the experiments (Lines 1, 4, and 7 of the plane view of Fig. 6). They are located along the central line and at 4 cm from each side of the channel. By identifying Y with the coordinate in the transversal direction (as shown in Fig. 6), the exact position of the sensor lines for Case A is shown in Table 4.

For the test case proposed, both the two-dimensional (2D) and 3D simulations obviously deliver an equivalent result given the applied boundary conditions. Even if this fact is obvious on a physical basis, it is less so for the numerical method used, particularly considering that the 3D mesh is unstructured and not identical for the 2D and 3D cases. The reason for introducing the benchmarking result is thus to verify that the proposed method yield the desired result.

Fig. 14 shows the comparison between experimental values measured at different Y-values and the correspondent numerical results. The 3D results for Case A1 confirm that the model slightly underestimates the experimental results for the pressure distribution. The overall numerical-experimental agreement is, however, noticeable.

A comparison between the 2D and 3D models was also performed for the unsteady regime at different times. The bottom pressure distribution is plotted in Figs. 15(a–d) for different time instances.

Case A2: 2D Coupled Model and Results

The coupled FSI model aims to simulating the seepage line and the free surface flow together with the evolution of the breach in the dam material. A typical FSI analysis is composed of two parts:
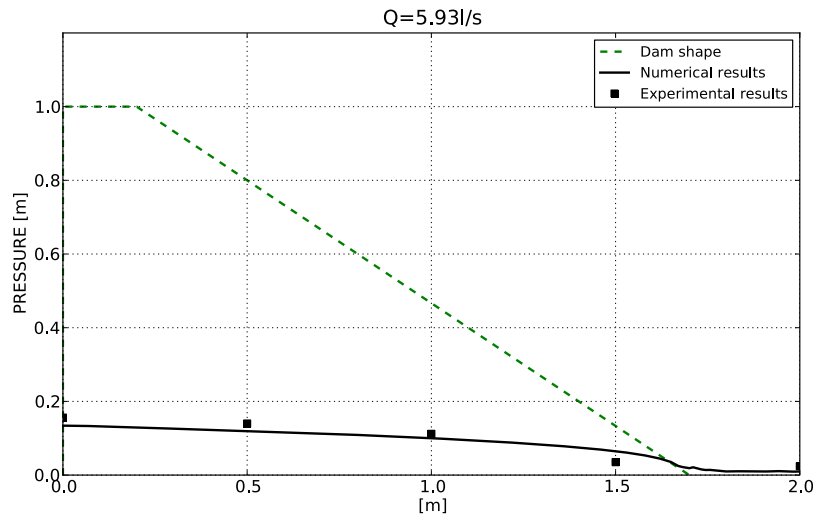

Fig. 27. Case B1a: bottom pressure distribution at stationary regime for $Q = 5.93$ L/s, porosity $n = 0.41$, $D_{50} = 35.04$ mm: numerical and experimental comparison
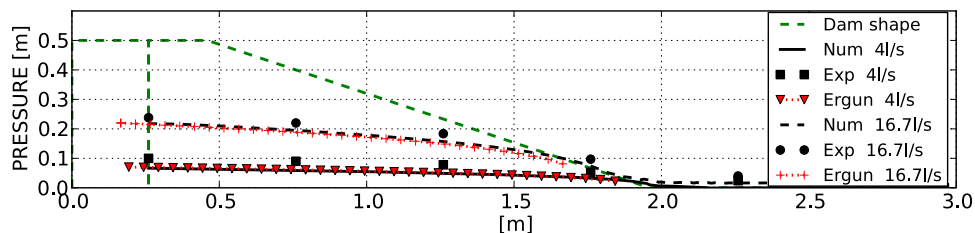

Fig. 28. Case B1b: bottom pressure distribution at stationary regime for $Q = 4$ L/s and $Q = 16.7$ L/s, porosity $n = 0.41$, $D_{50} = 35.04$ mm: numerical, experimental, and theoretical comparison
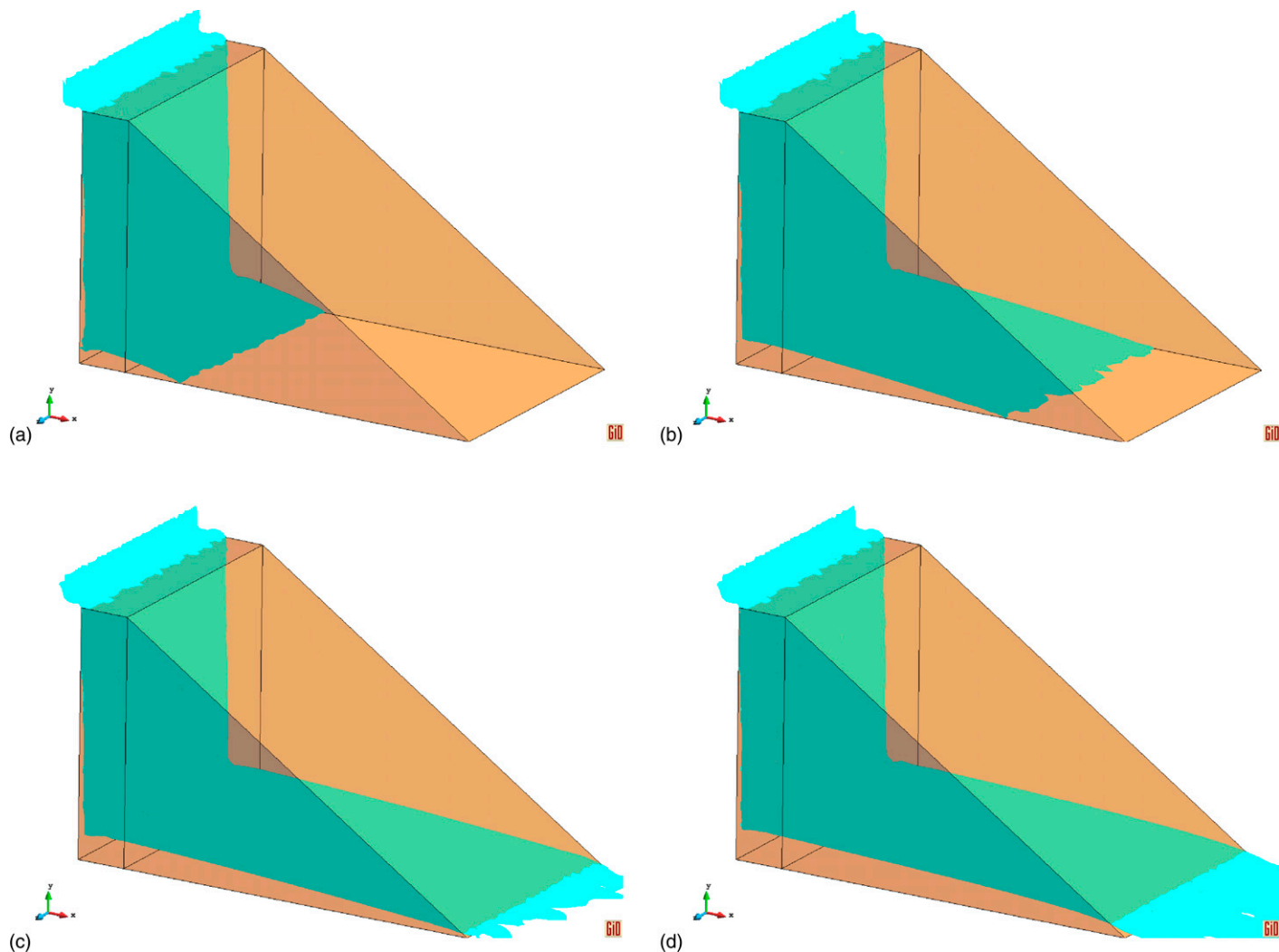
Fig. 29. Case B1a (3D): evolution of the seepage line in a dam with porosity $n = 0.41$, $D_{50} = 35.04$ mm, and $Q = 5.93$ L/s; (a) 5 s; (b) 10 s; (c) 15 s; (d) 145 s

- The fluid Eulerian model: Its construction is analogous to Case A1, and the mesh properties are the same. The main difference is the absence of any porous material. This information is passed by the PFEM model results during the calculation.
- The PFEM structural model: The dam model is constructed in a Lagrangian framework. This implies modeling only the material domain (i.e., the dam initial shape and the walls if present). The definition of a bounding box is required. A bounding box is the enclosing of the calculation domain. In Lagrangian problems, especially in CFD simulations, it is mandatory to limit the calculation domain because the nodes can freely move and may occupy progressively larger areas. It sets the analysis domain. If a node exits, the bounding box is no longer calculated, and it is deleted.

The advance of failure at every stage of the experiments is measured by the B parameter, which is by definition the horizontal projection of the position of the higher particle that moves. This movement is not quantified. In the present work, it was assumed that a particle moves if its total displacement is larger than the average dimension of the granular material (3.0 cm). This choice is arguable and, as it will be subsequently shown, it often makes our model too deformable. Nevertheless, this empirical criterion was used in all the models analyzed in this work to allow a comparative analysis.

Table 6. Case B1a: Meshes Used for the Analysis

Parameter	Mesh A	Mesh B	Mesh C	Mesh D
Dimension (m)	0.02	0.03	0.04	0.05
Number of elements	1,460,000	517,000	281,000	183,000
Number of nodes	250,000	89,600	49,000	34,000

In Fig. 16(a), schematic view of the fluid and structure boundary conditions is shown. The mesh used for the fluid model is the same as in Case A1, whereas for the structural model, the mesh has 3,400 three-noded linear triangular elements (Fig. 17).

The photogrammetric analysis of the A cases was also available and helped the comparison between experimental and numerical results. Fig. 18 shows on the lower part the digital model obtained by the photogrammetric analysis and on the upper part the contour fill of the displacements computed in our work. Displacements larger than 3 cm are marked with contour fill. The reason for this choice has been explained previously. Very good agreement is observed between the experimental and numerical advance of failure in the three cases. In Table 5, a comparison between the numerical (B_{num}) and the experimental (B_{exp}) advance of failure is provided.

Looking at the pressure head distribution for the three incoming discharges (Fig. 19), the experimental bottom pressure head is
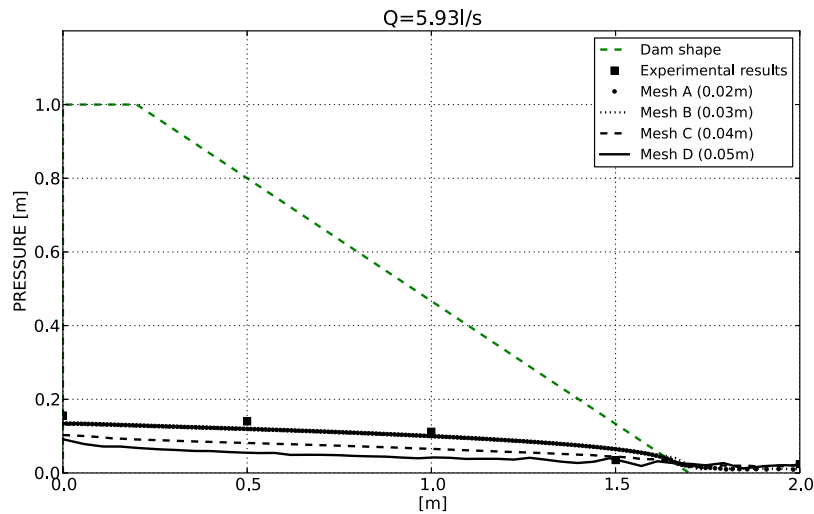
Fig. 30. Case B1a (3D): bottom pressure distribution at stationary regime for $Q = 5.93$ L/s, porosity $n = 0.41$, $D_{50} = 35.04$ mm; numerical, experimental, and theoretical comparison
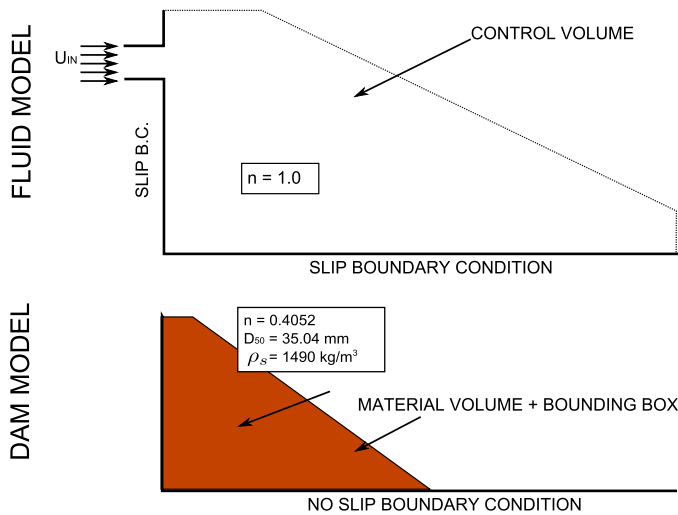

Fig. 31. Case B2: fluid and dam qualitative models and boundary conditions for the coupled analysis

Fig. 32. Case B2: 2D mesh of the dam model; 8,000 three-noded triangular elements

underestimated by the numerical one. This aspect is more relevant than in Case A1. This seems to indicate an internal variation of the material conditions (such as porosity or permeability) that is not taken into account by the model.

Fig. 19 also shows that in Case A2.3, the pressure head presents a lower experimental value in the region where water exits the dam. The contraction of the flux can be induced by the absence of the rockfill that flowed away during the failure process. This leads us to the conclusion that the failed material in the numerical model is more rigid than in the real case. Its accumulation over the toe of the dam induces a higher value of pressure than in the experiment.

Case A2: 2D Sequence of Incremental Discharges
The code developed in this work was conceived to analyze the consequence of transitory incoming discharges, allowing the use of flood curves as an input. This capability, however, has not been exploited in the examples presented, because the experimental results were given for the stationary regime, and no comparison can be made in the transitory regime.
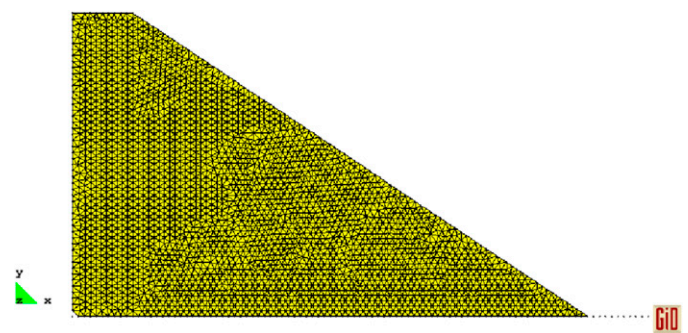
As a preliminary test, Cases A1–A2.1–A2.2 were run in sequence, leaving sufficient time for the intermediate stationary regime to be reached. The imposed curve representing the inlet discharge in function of time is reported in Fig. 20.

The pressure head for two pressure sensor locations is registered as shown in Fig. 21. The two points are located at 2.2 and 2.7 m from the upstream toe of the dam. The dotted line in the graph is the stationary value of pressure read from the piezometers in Cases A1, A2.1, and A2.2, respectively. Once more, the numerical results slightly underestimate the experimental ones, and the error is analogous to the one presented in the previous section.

Case A2: 3D Coupled Model and Results
Some preliminary 3D results were also obtained. The fluid and structural models were developed according to what was explained in the "Case A2: 2D Coupled Model and Results" section for the 2D validation case.

Nevertheless, the 3D deformation of the dam is not as clear as in the 2D case. This happens because the deformation is partially skewed by the remeshing process at each time step. Remeshing is a key point of PFEM. This method was originally conceived to treat Newtonian free surface problems where the regeneration of the mesh is required at each time step (Idelsohn et al. 2004). This is not the case for the present non-Newtonian algorithm where, in most of the steps,

all the nodes are in the unyielded region and do not move. For this reason, the possibility of inserting a conditional remeshing strategy should be added to have a viable 3D coupled FSI analysis code.

A preliminary tool that allows a conditional remeshing has already been inserted in the code and yields good results as the one shown in Fig. 22.

The plots of the pressure drop (Fig. 23) obtained with the 2D and 3D models (dotted and continuous line, respectively) are in good agreement with experimental values. This confirms the 3D results obtained in the "Case A1: Three-Dimensional Numerical Model and Results" section for Case A1, where only the fluid code was used.

Case B: Core Dam

The second experiment studied in this work is the seepage inside a core dam. The core is considered fixed and undeformable. The experiment is carried out by exclusively building the downstream slope as displayed in Fig. 24. The water entrance is set in the upper left part, omitting the simulation of the filling of the reservoir that is useless in the present analysis.

Case B: Experimental Setup and Geometry

The geometry of the dam is displayed in Fig. 25, where the distribution of the pressure sensors on the bottom of the channel can be seen.

The model is built to reproduce the real geometry of the experimental setup. Because the case of interest is the simulation of the

overtopped flow, the geometry of the model does not include the reservoir. The entrance of the water is set at the upper left part as shown in Fig. 26 (the arrows indicate the entrance of the water).

A slip boundary condition is imposed on the bottom of the channel and on the core side (bold lines in Fig. 26), whereas the upper left sides have an output condition (zero pressure).

Case B1a: 2D Numerical Model and Results

The mesh used for the calculation has 14,859 three-noded triangular elements. This is refined close to the critical zones of the falling of the water and near the bottom of the channel. The comparison between experimental and numerical pressure heads can be observed in Fig. 27.

Case B presents an additional difficulty in the fluid dynamic problem. It is particularly challenging to correctly simulate the falling jet of water (especially if the incoming water velocity is very slow) without suffering serious mass loss. The good agreement between experimental and numerical pressure heads confirms that this problem can be accurately modeled with the computational method developed in this work.

Cases B1b and B1c: Comparison with Theoretical Ergun Model

It has been observed that the numerical pressure head has lower values than the experimental ones. To verify if the problem can be attributed to the choice of the resistance law, a comparison with the

Fig. 33. Case B2a.1 ($Q = 19.36$ L/s): 2D comparison between experimental and numerical advance of failure; (a) experimental advance of failure $B_{exp} = 0.32$ m; (b) numerical advance of failure $B = B_{num} = 0.76$ m
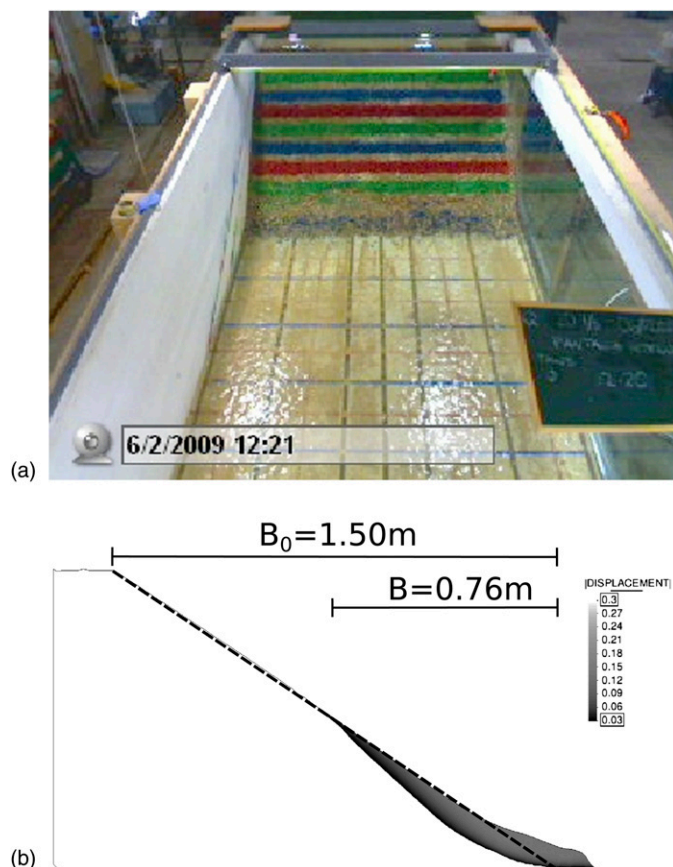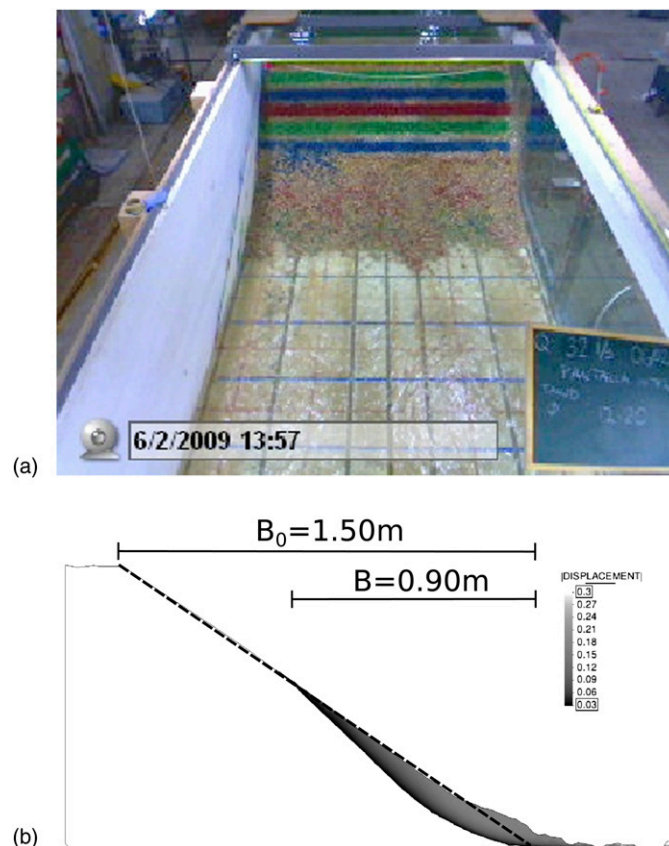

Fig. 34. Case B2a.2 ($Q = 30.45$ L/s): 2D comparison between experimental and numerical advance of failure; (a) experimental advance of failure $B_{exp} = 0.68$ m; (b) numerical advance of failure $B = B_{num} = 0.90$ m

theoretical results was performed following the work of López (2005). To do that, a slightly different geometry is analyzed. The dam studied is made of the same material as the one presented in the previous sections but its height is 0.5 m and the advance of the downstream slope is 1.5 m. The slope ratio is $3H{:}1V$.

The mesh used was composed of 2,865 nodes and 5,728 three-noded triangular elements.

The theoretical solution for an incoming discharge of 4 and 16.7 L/s is plotted in the dashed line with closed triangles and cross shapes in Fig. 28. The numerical approximation is very close to the Ergun theoretical one, as expected. Both these curves slightly underestimate the experimental values. This confirms that the Ergun model might not be the best choice for the resistance law of this kind of problem. To overcome this drawback, the authors plan to modify the code in the future to let the user insert a customized quadratic resistance law.

As a consequence of this observation, a permeameter for the rockfill was built to study this aspect and eventually derive an experimental resistance law for the materials.

Case B1a: 3D Numerical Model and Results

Fig. 29 shows a sequence of the transitory regime of the filling of the core dam using a 3D model. Three different meshes were used to analyze the sensitivity of the solution to the element dimension.

The characteristics of the four meshes considered are summarized in Table 6. The refinement is performed only in the dam volume, whereas the dimension of the elements is kept fixed in the rest of the domain.
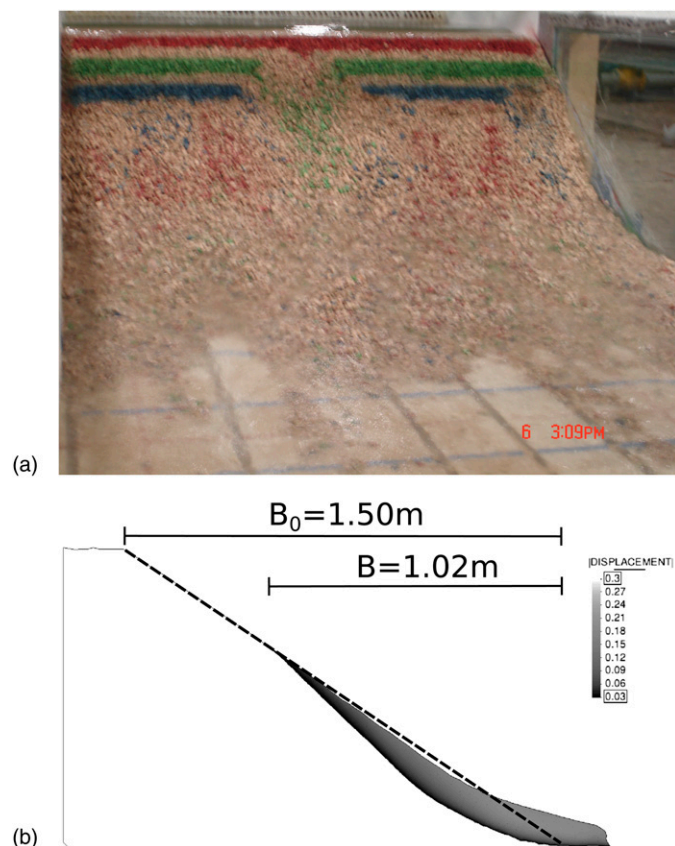

(a)

(b)

Fig. 35. Case B2a.3 ($Q = 39.56$ L/s): 2D comparison between experimental and numerical advance of failure; (a) experimental advance of failure $B_{exp} = 1.00$ m; (b) numerical advance of failure $B = B_{num} = 1.02$ m

Fig. 30 shows the pressure heads for the different mesh sizes. The convergence is achieved when the mesh is finer than 0.03 m. For larger meshes, the volume conservation is seriously compromised. This volume loss takes place when the flux falls down vertically. Therefore, particular care should be taken in the refinement of the mesh in this delicate area.

Case B2: Coupled Model and Results

The construction of the models for the coupled FSI case is analogous to what it was already explained in the "Case A2: 2D Coupled Model and Results" section for Case A2. A schematic representation of the boundary conditions can be seen in Fig. 31. Fig. 32 shows the Lagrangian mesh used in the calculation. It has 8,000 three-noded triangles.

Case B2

Figs. 33–35 show the comparison between experimental and numerical dam deformation at each step of discharge for $\phi' = 41°$. The error in the evaluation of B is progressively reduced when the discharge increases as detailed in Table 7.

An additional consideration can be made by looking at the pressure head distribution of the three cases shown in Fig. 36. As for Case A2, the amount of moved rockfill is lower in the simulation than in the experiments. The higher value of numerical pressure at the toe of the dam indicates that granular material is present over the sensor position, i.e., the resistance given by the grains increases the water level and the pressure head as well. This indicates that the material settles faster than in the experiment. This may be corrected with the insertion of an algorithm that take into account the superficial dragging induced by water.

Conclusions and Future Work

In this work, a new approach for the simulation of the failure of downstream slopes in rockfill dams was presented and validated. The model allows the simultaneous analysis of the dynamic evolution of seepage and the free surface flow both upstream and downstream the dam. This is done by an Eulerian code developed in this work, which uses a unified formulation for the seepage and the fluid flow in the vicinity of the dam. The structural response of the rockfill material is evaluated with a viscorigid constitutive model that makes use of a Mohr-Coulomb failure criterion. The rockfill is treated as a highly viscous non-Newtonian fluid whose viscosity drastically decreases when, because of the hydrodynamic forces, the yield stress is exceeded. When this happens, failure occurs and granular flow of the rockfill material is generated. Finally the fluid-structure coupling is performed using a fully staggered scheme and a mapping algorithm between nonmatching Eulerian and Lagrangian meshes.

The model was validated using the results of an experimental campaign on small-scale dams, proving that the algorithm accurately reproduces both the fluid and coupled problem. The main considerations for the fluid module are as follows:

Table 7. Case B2: Comparison between Experimental (B_{exp}) and Numerical (B_{num}) Advance of Failure for $\phi' = 41°$

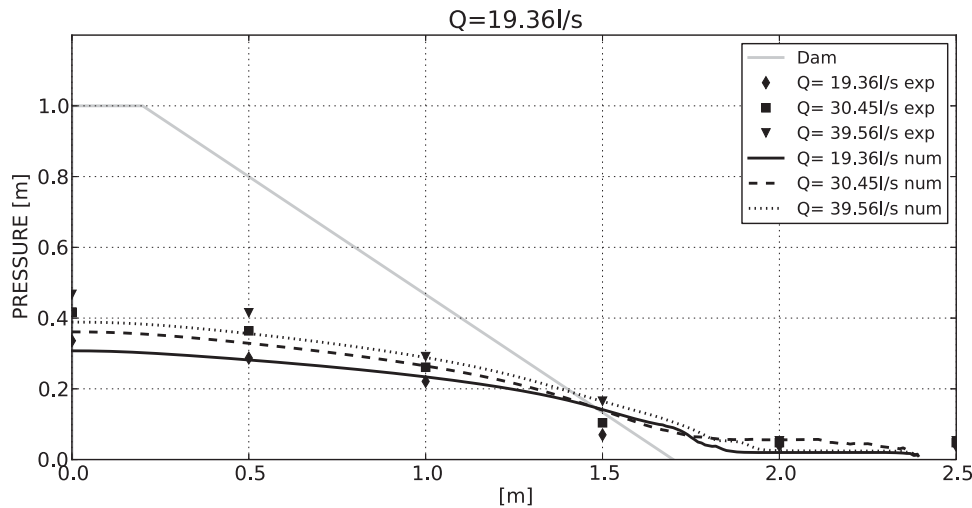| Case	Q (L/s)	B_{exp}	B_{num}	Error (%)
B2a.1	19.36	0.32	0.76	137
B2a.2	30.45	0.68	0.90	32
B2a.3	39.56	1.00	1.02	2

Fig. 36. Bottom pressure distribution at stationary regime for Case B2a.1, B2a.2, and B2a.3, respectively (porosity $n = 0.41$, $D_{50} = 35.04$ mm); numerical and experimental comparison

1. There is a good agreement between experimental and numerical pressure heads for the undeformed cases (A1 and B1) both in 2D and 3D. Nevertheless, the numerical results always slightly underestimate the experimental values. Additional numerical experiments carried out by the authors can confirm that the pressure line is always lower than the experimental one, especially when increasing the porosity values. This aspect, together with the comparison with theoretical Ergun curves shown in the "Cases B1b and B1c: Comparison with Theoretical Ergun Model" section, leads to the conclusion that the Ergun coefficients slightly underestimate the pressure drop in the seepage problem. In the future, a general quadratic Darcy law ($\alpha u + \beta u^2$) will be used, and the choice of the suitable α and β coefficients will be left to the user.
2. The overestimation of the pressure head at the toe of the deformed dam (Cases A2 and B2) might be the consequence of a smaller deformation of the failed material. Whereas the advance of failure is correctly reproduced, the failed material settles faster than in the real case and accumulates close to the original toe. In the experiments, the path run by the failed rockfill material is much larger. This can be avoided with the insertion of an erosion algorithm.
3. The code also has good performance in the complex case of a falling jet of water.
4. Another challenging aspect of Cases A1 and B1 is that the discharges are very low. This might represent a problem at the beginning of the simulation when a very thin layer of water starts filling the dam. This issue is avoided by refining the mesh close to the bottom.

Considerations for the coupled FSI module are as follows:

1. The FSI code reproduces the incremental failure of the dam as the overspilling discharge increases. It represents correctly the crucial cases for which failure achieves the crest of the dam. On the contrary, for lower discharges, B is overestimated. This aspect is also reflected at the experimental level. In fact, when repeating the same experiment, the onset of the breaching suffers from a certain data scatter. Conversely, the discharge for which the failure reaches the crest is always the same.
2. As observed in the conclusions regarding the fluid module, the failed material settles faster than in the real case. This can be

a consequence of the chosen viscorigid constitutive model. In fact, when the shear stress decreases under the yield stress threshold, the viscosity dramatically increases, causing a sudden stop of the nodes motion. The authors plan to develop an erosion tool that will solve this problem by dragging away the deposed material.

Acknowledgments

References

Biot, M. A. (1941). "General theory of three-dimensional consolidation." *J. Appl. Phys.*, 12(2), 155–164.

Biot, M. A. (1955). "Theory of elasticity and consolidation for a porous anisotropic solid." *J. Appl. Phys.*, 26(2), 182–185.

Butler, K., Oñate, E., Idelsohn, S., and Rossi, R. (2007). "Modeling polymer melt flow using the particle finite element method (PFEM)." *Proc., 11th Int. Interflam Conf. 2007*, Vol. 2, Interscience Communications, London, 929–940.

Campos, H., Morán, R., and Toledo, M. (2010). "Estudio de la rotura de presas de material granular grueso uniforme no cohesivo sin elemento impermeable. Fase de inicio." *Dam maintenance and rehabilitation II*, CRC Press, Boca Raton, FL, 599–608 (in Spanish).

Carbonell, J. M., Oñate, E., and Suárez, B. (2010). "Modeling of ground excavation with the particle finite-element method." *J. Eng. Mech.*, 10.1061/(ASCE)EM.1943-7889.0000086, 455–463.

Chanson, H. (2009). "Embankments overflow protection system and earth dam spillways." Chapter 4, *Dams: Impacts, stability and design*, W. P. Hayes and M. C. Barnes, eds., Nova Science Publishers, Hauppauge, NY, 101–132.

Chen, Y., Hu, R., Lu, W., Li, D., and Zhou, C. (2011). "Modeling coupled processes of non-steady seepage flow and non-linear deformation for a concrete-faced rockfill dam." *Comput. Struct.*, 89(13–14), 1333–1351.

Chorin, A. J. (1967). "A numerical method for solving incompressible viscous flow problems." *J. Comput. Phys.*, 2(1), 12–26.

Codina, R. (2001). "Pressure stability in fractional step finite element methods for incompressible flows." *J. Comput. Phys.*, 170(1), 112–140.

Coussy, O. (1995). *Mechanics of porous media*, Wiley, New York.

Cremonesi, M., Frangi, A., and Perego, U. (2011). "A Lagrangian finite element approach for the simulation of water-waves induced by landslides." *Comput. Struct.*, 89(11–12), 1086–1093.

Dadvand, P., Rossi, R., and Oñate, E. (2010). "An object-oriented environment for developing finite element codes for multi-disciplinary applications." *Arch. Comput. Meth. Eng.*, 17(3), 253–297.

de Boer, R. (2000). *Theory of porous media*, Springer, Berlin.

Discacciati, M., Miglio, E., and Quarteroni, A. (2002). "Mathematical and numerical models for coupling surface and groundwater flows." *Appl. Numer. Math.*, 43(1–2), 57–74.

Dolezalova, M., and Hladik, I. (2011). "Constitutive models for simulation of field performance of dams." *Int. J. Geomech.*, 10.1061/(ASCE) GM.1943-5622.0000039, 477–489.

Donea, J., and Huerta, A. (2003). *Finite elements methods for flow problems*, Wiley, New York.

Faeh, R. (2007). "Numerical modeling of breach erosion of river embankments." *J. Hydraul. Eng.*, 10.1061/(ASCE)0733-9429(2007) 133:9(1000), 1000–1009.

Froehlich, D. C. (2008). "Embankment dam breach parameters and their uncertainties." *J. Hydraul. Eng.*, 10.1061/(ASCE)0733-9429(2008)134: 12(1708), 1708–1721.

Fu, J. F., and Jin, S. (2009). "A study on unsteady seepage flow through dam." *J. Hydrodyn. Ser. B*, 21(4), 499–504.

Hansen, D. (1992). "The behaviour of flowthrough rockfill dams." Ph.D. thesis, Univ. of Ottawa, Ottawa.

Hansen, D., and Roshanfekr, A. (2012). "Assessment of potential for seepage-induced unraveling failure of flow-through rockfill dams." *Int. J. Geomech.*, 10.1061/(ASCE)GM.1943-5622.0000145, 560–573.

Idelsohn, S. R., Oñate, E., and Del Pin, F. (2004). "The particle finite element method: A powerful tool to solve incompressible flows with free-surfaces and breaking waves." *Int. J. Numer. Methods Eng.*, 61(7), 964–989.

International Commission on Large Dams (ICOLD). (1995). "Dam failures statistical analysis." *Bulletin 99*, Paris.

Khoshghalb, A., and Khalili, N. (2010). "A stable meshfree method for fully coupled flow-deformation analysis of saturated porous media." *Comput. Geotech.*, 37(6), 789–795.

KRATOS [Computer software]. Barcelona, Spain, CIMNE.

Larese, A. (2012). "A coupled Eulerian-PFEM model for the simulation of overtopping in rockfill dams." Ph.D. thesis, Univ. Politècnica de Catalunya (UPC BarcelonaTech), Barcelona, Spain ⟨http://hdl.handle.net/10803/108502⟩.

Larese, A., Rossi, R., and Oñate, E. (2011a). "Coupling Eulerian and Lagrangian models to simulate seepage and evolution of failure in prototype rockfill dams." *Proc., XI ICOLD Benchmark Workshop on Numerical Analysis of Dams*, SpanCOLD, Madrid, Spain.

Larese, A., Rossi, R., and Oñate, E. (2011b). "Theme B: Simulation of the behavior of prototypes of rockfill dams during overtopping scenarios: Seepage evolution and beginning of failure." *Proc., XI ICOLD Benchmark Workshop on Numerical Analysis of Dams*, SpanCOLD, Madrid, Spain.

Larese, A., Rossi, R., Oñate, E., and Idelsohn, S. (2008). "Validation of the particle finite element method (PFEM) for simulation of free surface flows." *Eng. Comput.*, 25(4), 385–425.

Larese, A., Rossi, R., Oñate, E., and Idelsohn, S. (2012). "A coupled PFEM-Eulerian approach for the solution of porous FSI problems." *Comput. Mech.*, 50(6), 805–819.

Larese, A., Rossi, R., Oñate, E., and Toledo, M. (2010). "Physical and numerical modelization of the behavior of rockfill dams during over-topping scenarios." *Dam maintenance and rehabilitation II*, CRC Press, Boca Raton, FL, 479–487.

Lechuga, C., et al. (2010). "Estudios sobre el comportamiento de presas de escollera ante vertidos por coronación." *Proc., IX Jornadas Españolas de presas*, SpanCOLD, Madrid, Spain (in Spanish).

Lewis, R., and Schrefler, B. (1998). *The finite element method for the static and dynamic deformation and consolidation of porous media*, Wiley, New York.

Li, B. (1995). "Flowthrough and overtopped rockfill dams." Ph.D. thesis, Univ. of Ottawa, Ottawa.

López, J. (2005). "Caracterización del Proceso de Saturación de una Presa de Escollera Mediante Métodos Unidimensionales." M.Sc., Univ. Politécnica de Madrid, Madrid, Spain (in Spanish).

Marti, J., Ryzhakov, P., Idelsohn, S., and Oñate, E. (2012). "Combined Eulerian-PFEM approach for analysis of polymers in fire situations." *Int. J. Numer. Methods Eng.*, 92(9), 782–801.

Mier, M., Idelsohn, S., and Oñate, E. (2011). "Advances in the simulation of multi-fluid flows with the particle finite element method." *Int. J. Numer. Methods Fluids*, 67(11), 1516–1539.

Morán, R., and Toledo, M. (2011). "Research into protection of rockfill dams from overtopping using rockfill downstream toes." *Can. J. Civ. Eng.*, 38(12), 1314–1326.

Nield, D., and Bejan, A. (1992). *Convection in porous media*, Springer, New York.

Nithiarasu, P., Seetharamu, K. N., and Sundararajan, T. (1997). "Natural convective heat transfer in a fluid saturated variable porosity medium." *Int. J. Heat Mass Transfer*, 40(16), 3955–3967.

Oñate, E., et al. (2011a). "Advances in the particle finite element method (PFEM) for solving coupled problems in engineering." *Particle-based methods, computational methods in applied sciences*, E. Oñate and R. Owen, eds., Vol. 25, Springer, New York, 1–49.

Oñate, E., Celigueta, M. A., Idelsohn, S. R., Salazar, F., and Suarez, B. (2011b). "Possibilities of the particle finite element method for fluid-soil-structure interaction problems." *J. Comput. Mech.*, 48(3), 307–318.

Oñate, E., García, J., Idelsohn, S. R., and Del Pin, F. (2006). "Finite calculus formulations for finite element analysis of incompressible flows. Eulerian, ALE and Lagrangian approaches." *Comput. Methods Appl. Mech. Eng.*, 195(23–24), 3001–3037.

Oñate, E., Idelsohn, S. R., Celigueta, M. A., and Rossi, R. (2008). "Advances in the particle finite element method for the analysis of fluid-multibody interaction and bed erosion in free surface flows." *Comput. Methods Appl. Mech. Eng.*, 197(19–20), 1777–1800.

Oñate, E., Idelsohn, S. R., Del Pin, F., and Aubry, R. (2004). "The particle finite element method—An overview." *Int. J. Comput. Methods*, 1(2), 267–307.

Osher, S., and Fedkiw, R. (2003). *Level set methods and dynamic implicit surfaces*, Springer, New York.

Papanastasiou, T. C. (1987). "Flows of materials with yield." *J. Rheol.*, 31(5), 385–404.

Rossi, R., Larese, A., Dadvand, P., and Oñate, E. (2013). "An efficient edge-based level set finite element method for free surface flow problems." *Int. J. Numer. Methods Fluids*, 71(6), 687–716.

Ryzhakov, P., Rossi, R., Idelsohn, S., and Oñate, E. (2010). "A monolithic Lagrangian approach for fluid-structure interaction problems." *Int. J. Comput. Mech.*, 46(6), 883–899.

Salazar, F., Oñate, E., and Morán, R. (2012). "Modelación numérica de deslizamientos de laderas en embalses mediante el método de partículas y elementos finitos (PFEM)." *Revista Int. dem Métodos Numéricos para Cálculo y Diseño en Ingeniería*, 28(2), 112–123 (in Spanish).

Spanish Association for Standardization and Certification (AENOR). (2007). "Test methods for natural stone—Determination of true density and apparent density, and of total and open porosity." *UNE-EN 1936*, Madrid, Spain.

Spanish Association for Standardization and Certification (AENOR). (2012). "Tests for geometrical properties of aggregates—Part 1: Determination of particle size distribution—Sieving method." *UNE-EN 993-1*, Madrid, Spain.

Témam, R. (1969). "Sur l'approximation de la solution des équations de Navier-Stokes par la méthode des pas fractionaires (I)." *Arch. Ration. Mech. Anal.*, 32(2), 135–153 (in French).

Toledo, M. (1997). "Presas De Escollera Sometidas a Sobrevertido. Estudio del Movimientos dal Agua a Través de la Escollera e de la Estabilidad Frente al Deslizamiento en Masa." Ph.D. thesis, Univ. Politécnica de Madrid, Madrid, Spain (in Spanish).

Toledo, M. (1998). "Safety of rockfill dams subject to overtopping." *Proc., Int. Symp. on New Trends and Guidelines on Dam Safety*, L. Berga, ed., Taylor & Francis, London.

Toledo, M., Moremo, J., and Mateos, C. (2004). "Physical and mathematical modelling of embankment dam failure due to overtopping." *Proc., Int. Seminar on Stability and Breaching of Embankment Dams*, Oslo, Norway.

Urquiza, J. M., N'Dri, D., Garon, A., and Delfour, M. C. (2008). "Coupling Stokes and Darcy equations." *Appl. Numer. Math.*, 58(5), 525–538.

Varadarajan, A., Sharma, K. G., Abbas, S. M., and Dhawan, A. K. (2006). "Constitutive model for rockfill materials and determination of material constants." *Int. J. Geomech.*, 10.1061/(ASCE)1532-3641(2006)6: 4(226), 226–237.

Wang, Z., and Bowles, D. S. (2006). "Dam breach simulations with multiple breach locations under wind and wave actions." *Adv. Water Resour.*, 29(8), 1222–1237.

Zienkiewicz, O. C., and Shiomi, T. (1984). "Dynamic behaviour of saturated porous media: The generalized Biot formulation and its numerical solution." *Int. J. Numer. Anal. Methods Geomech.*, 8(1), 71–96.